Iranian Journal of Astronomy and Astrophysics
Vol. 12, No. 1, Winter 2025, 37–71
©Available online at http://ijaa.du.ac.ir
DOI: 10.22128/ijaa.2025.1013.1212
Online ISSN: 2383–403X

Iranian Journal of Astronomy and Astrophysics

Review Paper

Applications of Image Processing Methods in Solar Coronal Data Analyzes: An Overview

Mohsen Javaherian*[1] · Seyed Alireza Bashiri Mosavi[2] · Parsa Mohammadi[3] · Zahra Eskandari[4]

[1] Research Institute for Astronomy and Astrophysics of Maragha (RIAAM), University of Maragheh, Maragheh, P.O. Box: 55134–441, Iran;
*email: javaherian@maragheh.ac.ir

[2] Department of Electrical and Computer Engineering, Buein Zahra Technical University, Buein Zahra, Qazvin, Iran;
email: abashirimosavi@bzte.ac.ir

[3] Department of Electrical and Computer Engineering, Buein Zahra Technical University, Buein Zahra, Qazvin, Iran;
email: parssamohammadi@gmail.com

[4] Department of Geography and Rural Planning, University of Zanjan, University Blvd., 45371–38791, Zanjan, Islamic Republic of Iran;
email: z.eskandari@znu.ac.ir

Received: 17 May 2025; **Accepted:** 13 August 2025; **Published:** 26 August 2025

Abstract. The solar corona, the outermost layer of the Sun's atmosphere, plays a crucial role in understanding solar phenomena and their impact on space weather and terrestrial systems. As advancements in solar observation technologies continue to produce high-resolution coronal images, the need for effective image processing methods has become increasingly important. This paper highlights the significance of processing techniques specifically designed for solar coronal images, which are essential for revealing intricate details of coronal structures, such as solar flares, coronal mass ejections, and magnetic field configurations. We explore various image processing methodologies, including event detection, contrast enhancement, and pattern analysis, that enhance the quality and interpretability of coronal images. Additionally, we address the challenges associated with processing coronal images, such as the presence of unrelated background, variability in data acquisition, and the complexity of coronal dynamics. By reviewing recent advancements in new instruments and algorithms, this paper explains how improved technologies and developed processing methods can lead to more accurate analyses of coronal phenomena, ultimately contributing to the broader field of solar research and our understanding of the Sun's influence on the solar system. The findings emphasize the need for ongoing innovation in image processing methods to unlock new insights into the behavior of the solar corona and its implications for space weather forecasting and solar-terrestrial interactions.

Keywords: Sun: Corona, Sun: Activity, Sun: Magnetic Fields, Sun: Active Regions, Sun: Coronal Holes, Sun: Coronal Loops, Techniques: Image Processing.

1 Introduction

The corona, with its complex structure and dynamic magnetic fields, provides considerable challenges and opportunities for understanding physics of the Sun, especially using mag-

* *Corresponding author*

netohydrodynamic (MHD) theory [1]. The corona has undeniable effects on space weather through solar wind, flares, and coronal mass ejections (CMEs). These types of phenomena disrupt Earth's magnetosphere, disturb satellites and infrastructure, and turn out auroras, while changing the interplanetary medium and radiation risks beyond Earth. Studying this Sun-Earth-space connection is crucial for predicting space weather hazards, developing instruments, and advancing both astrophysical knowledge and human endeavors in space exploration (e.g., see [2–5]). Addressing critical questions about the physics of the corona through manual and/or automated techniques is vital, including modeling coronal loops, understanding heating mechanisms in different regions with various temperatures, analyzing acceleration processes of particles generated from different solar wind types, and surveying the global maps of the corona's magnetic field [6,7] associated with its local structures and evolutions [8,9].

The word "corona" means "crown" in Latin and describes the faint halo seen around the Sun during total solar eclipses (e.g., [10]). This halo is made of very hot, thin plasma (millions of degrees Kelvin) and glows about as brightly as a full Moon. People have observed the corona for hundreds of years, and ancient civilizations revered the Sun. For example, Egyptians worshipped it, as shown by a design resembling the corona on King Tut's chair [11], while ancient Chinese thought eclipses were caused by a dragon eating the Sun and employed astronomers to fight it [12,13].

Historically, observing the corona in white light was only possible during rare, brief total solar eclipses because the photosphere is vastly brighter. This limitation led to the invention of the coronagraph [14], which uses an occulting disk to block the Sun's face, enabling regular ground-based observations [14,15]. Space-based coronagraphs (e.g., Skylab, SMM, SoHO [16], STEREO) greatly reduce stray light. The corona can also be directly observed in soft X-rays and extreme ultraviolet (EUV) from space (missions like Skylab, Yohkoh, TRACE, SoHO, Hinode, SDO; e.g., [16–20]) since Earth's atmosphere blocks these wavelengths. The eclipse corona forms when light from the Sun's surface scatters off free electrons (called the K-corona) and dust particles (called the F-corona) (e.g., [21,22]). Close to the Sun (within about 2.3 solar radii), the K-corona dominates. Its brightness shows where the electron density is highest. As seen in Figure 1, the corona's structures during an eclipse are shaped by the Sun's magnetic field: loops trap plasma closer to the surface, while open field lines are stretched out by the solar wind [23]. A major advance in understanding the corona happened in the 1930s. Scientists found that many unusual light patterns (spectral lines) seen in the corona came from known elements in extremely ionized states. This showed the corona's temperature must be several million Kelvin – hot enough to strip away most electrons from atoms, even heavy ones. Because of this intense heat, the corona gives off X-rays, allowing it to be seen directly in soft X-rays or EUV light using space telescopes [15].

The inner corona's electron density is typically around a few times $10^{14}\mathrm{m}^{-3}$ but can be 5–20 times higher in some areas. It drops sharply with distance from the Sun, falling to a few times $10^{12}\mathrm{m}^{-3}$ at one solar radius above the surface and below $10^{10}\mathrm{m}^{-3}$ at ten solar radii. Explaining how the corona and chromosphere get so hot is a major challenge in solar physics. Two leading theories involve magnetic waves carrying energy from below or magnetic reconnection events [24,25]. Evidence for both waves (like Alfvénic waves) and reconnection exists.

The corona experiences significant energy losses due to thermal conduction, radiation, and mass outflow, with a total energy loss of approximately 10^{21} W, which constitutes only 0.001% of the solar luminosity, estimated at 3.86×10^{26} W. Coronal magnetic fields range from a few to hundreds of Gauss and can be measured via radio waves or infrared line splitting (e.g., [26]), allowing comparison with models [27,28]. We should note that the

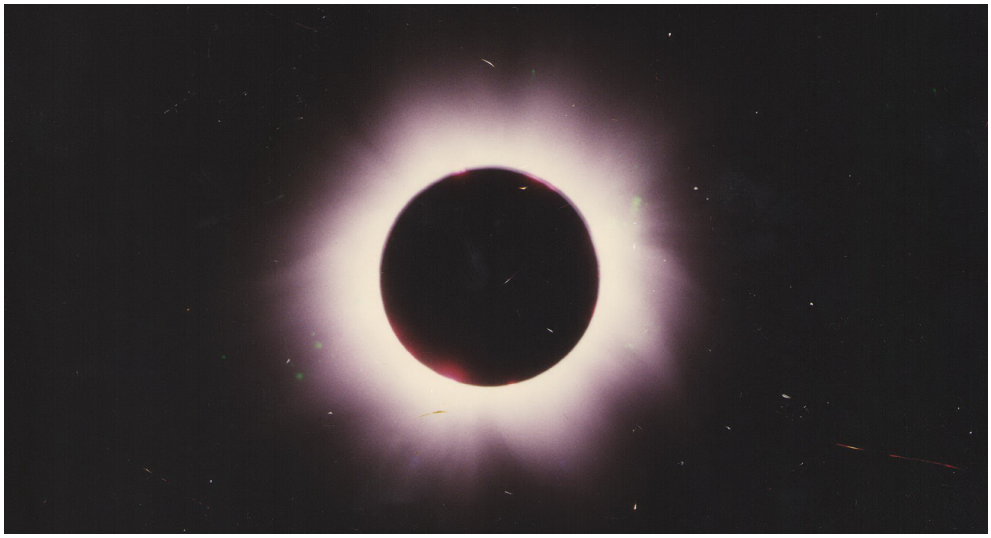

Figure 1: The solar corona was observed during the eclipse on August 11, 1999, in Isfahan, Iran. The data is selected from a collection of photographs archived by Iraj Safaei (with the permission).

corona's shape, magnetic fields, and temperature change with the solar cycle [29,30]. At sunspot maximum, streamers and CHs are spread across latitudes. At minimum, streamers cluster near the equator while CHs dominate the poles (see [31–33]).

The corona's global structure is divided into three main components based on magnetism and radiation: Active regions (ARs) which are included areas of strong magnetic fields (1–4 MK), sunspots, and frequent eruptions. Quiet Sun (QS) which are areas of weaker, diffuse closed magnetic fields, still dynamic. Coronal holes (CHs) which are darker areas of open magnetic fields, sources of the fast solar wind. This structure reflects the balance between magnetic energy storage, release, and connection to space [25,34].

Locally, main structures include dark CHs (open fields), bright coronal loops (closed fields connecting opposite polarities), and small X-ray bright points (tiny magnetic loops; e.g., [35]). A prominent feature is the coronal (helmet) streamer, a bright, dense structure extending above the limb. It forms over prominences or ARs, with closed magnetic fields at the base transitioning to open fields stretched by the solar wind, resembling a helmet [36,37]. MHD models exist [38,39]. There are two main types: 1- Bipolar Streamers: Above a single bipolar arcade, between opposite-polarity CHs. 2- Unipolar (Pseudo) Streamers: Separate CHs of the same polarity, above a quadrupolar field [40,41].

Readers may consult reviews and dissertations covering interesting solar corona topics for deeper exploration. These include: waves and oscillations in solar corona [42–48], the coronal heating [34,49], Kinematic properties of waves in the solar corona and its kinetic physics [50,51], ARs [52,53], CHs [31,33], flares [54–56], CMEs [57–61], and coronal bright points (CBPs) [62–64].

Several solar phenomena, including flares, are systematically documented in dedicated catalogs. For instance, solar flare events are cataloged in different resources. For instance, the Geostationary Operational Environmental Satellite (GOES) Flare Catalog maintained by NOAA, is the definitive record of solar flares detected via X-ray flux measurements from GOES satellites since 1975 [65–67]. It classifies flares by peak X-ray intensity

(e.g., X, M, C-class) and provides start, peak, and end times of flares with their locations (https://umbra.nascom.nasa.gov/goes/). The other known example is the Hinode Flare Catalog [68]. The Hinode Flare Catalog documents solar flares observed by the Hinode satellite. It combines high-resolution data from Hinode's instruments – the Solar Optical Telescope (SOT), X-Ray Telescope (XRT), and EUV Imaging Spectrometer (EIS) – to provide detailed flare characteristics, including timing, location, magnetic field evolution, and multi-wavelength imagery. This catalog complements broader flare databases (e.g., GOES) by emphasizing fine-scale processes, such as magnetic reconnection dynamics and plasma heating (https://hinode.isee.nagoya-u.ac.jp/flare_catalogue/). The Astro-rivelatore Gamma a Immagini LEggero (AGILE) Flare Catalog [69] is one of the new ones that records high-energy solar flares detected by the Italian AGILE satellite (launched 2007), specializing in gamma-ray and hard X-ray observations. It focuses on impulsive solar events, providing timing, spectral data, and localization of flares, particularly those associated with particle acceleration and gamma-ray emissions. Also, this catalog complements softer X-ray flare databases (e.g., GOES) by capturing rare and high-energy processes (https://www.ssdc.asi.it/agilesolarcat/). The other database is Archival Solar flaRes Catalog (ASR) [70] which is not widely used in literatures. The ASR catalog is publicly available at (https://github.com/helio-unitov/ASR_cat).

The other useful database is the Solar Demon database (e.g., see [71,72]). Solar Demon is an automated, real-time solar feature detection system designed to identify and track dynamic events in the Sun's atmosphere using EUV imagery from the SDO. It specializes in detecting phenomena such as Solar flares, Coronal dimmings, Coronal jets, EIT waves (large-scale propagating disturbances). The database archives event detections, metadata, and processed imagery, serving as a resource for solar physics research and space weather forecasting. It also involves real-time processing (analyzes SDO/AIA data streams in near-real time with the cadence of 1 – 2 minutes), multi-event detection (simultaneously tracks flares, dimmings, jets, and EIT waves using tailored algorithms), event catalogs (Provides timestamps, locations, intensities, and morphological data for each detected event), and data products (includes EUV images, difference maps, and event overlays for visualization). Solar Demon employs thresholding, segmentation, and temporal tracking for solar activity detection: for flare detection, it monitors EUV intensity spikes and triggers alerts when thresholds exceed baseline levels. Coronal dimmings are identified by tracking rapid EUV intensity drops post-flare/CME and mapping regions via running difference images. EIT waves are detected using spatiotemporal filtering to capture propagating brightenings/dimmings, while collimated plasma jets are recognized through morphological filters analyzing ejection patterns. To access the data, refer to the Solar Demon website (https://www.sidc.be/SolarDemon/).

Image segmentation partitions an image into meaningful regions sharing similar attributes. Thresholding is the simplest method, separating pixels based on intensity values relative to a chosen threshold. Otsu's method (1979) automates this by maximizing inter-class variance [73]. Edge-based segmentation identifies boundaries using gradient operators like the Canny edge detector (1986), which optimizes noise reduction and edge localization [74]. Region-based methods like seeded region growing [75] group adjacent pixels with homogeneous properties, while clustering algorithms such as k-means (e.g., see [76] and references therein) partition pixels into clusters based on feature space similarity. Watershed segmentation [77] treats images as topographic maps, flooding basins from minima to separate regions. These classical methods are computationally efficient but often struggle with noise, intensity inhomogeneity, and complex textures.

To address limitations of classical techniques, active contour models ([78] and references therein) evolve curves under energy constraints to fit object boundaries. Graph-based segmentation like normalized cuts [79] models pixel relationships as graphs, partitioning

them by minimizing edge weights between groups. The rise of deep learning revolutionized segmentation: Convolutional Neural Networks (CNNs) like U-Net (e.g., see [80] and references therein) use encoder-decoder architectures with skip connections for precise biomedical segmentation. Instance segmentation methods (e.g., Mask R-CNN; [81]) extend CNNs to identify object instances and their pixel-level masks. Transformer-based architectures (e.g., Transformer Networks; [82]) capture global context more effectively than CNNs. These methods excel with complex data but require large labeled datasets and significant computational resources.

As we deal with stream of solar data, this is undeniable to make a connection between two fields of image processing and solar physics. As an example, solar imagery – particularly from instruments like SDO/AIA [83], SOHO/LASCO [84], and Hinode/XRT [85] – presents unique challenges: low contrast between coronal structures, dynamic intensity ranges, and complex magnetic topology. Classical methods like multiscale thresholding [73] and region growing [75] are used to isolate ARs [86] but often fail with faint coronal loops. Edge-based techniques [74] help detect CH boundaries [87]. New methods now dominate for segmenting solar flares [88], CHs [89], and CMEs [90], leveraging their ability to learn hierarchical features from multi-wavelength data. These advancements enable precise tracking of magnetic activity and space weather forecasting.

Before we explore the review of coronal image processing, we briefly summarize the significance of pre-processing methods for solar images, as detailed in an article provided by Javaherian and Eskandari (2023) [91] (the interested reader also can find the details about some studies in [92,93] and references therein). The role of image preprocessing techniques in solar image analysis is crucial for effectively applying automated feature detection algorithms. These procedures are designed to remove unwanted features, correct artifacts, enhance significant structures, and standardize images for further analysis. Key aspects of these pre-processing methods include correcting instrumental effects such as dark and hot pixels from charge-coupled devices (CCDs), suppressing non-solar artifacts like cosmic rays, and ensuring sufficient image resolution through deconvolution or resampling. Moreover, background subtraction, coordinate system alignment, and various image filtering techniques are essential steps for improving feature detection accuracy. Techniques like speckle imaging and phase diversity are utilized for image restoration, especially in ground-based observations that are influenced by atmospheric distortions. The article also outlines specific preprocessing tasks necessary for tracking features in sequential frames, including derotation and the application of subsonic filters. By carefully addressing these factors, researchers can greatly enhance the reliability and accuracy of their analyses of solar images. The paper is organized as follows: We explained some main telescopes and instruments used for studying the solar corona in Section 2. The types of solar coronal data are described in Section 3. We present image processing methods in solar coronal data in Section 4. Concluding remarks are given in Section 5.

2 Some Main Telescopes and Instruments for Studying the Solar Corona

Here, we present some of the primary telescopes and instruments used to study the solar corona. It's a combination of diverse observatories that collaborate to provide us with the clearest view of the Sun's outer atmosphere. This incredible partnership utilizes advanced technology, both on Earth and in space.

2.1 Space-Based Telescopes and Instruments

Space-based telescopes are advantageous because they bypass the Earth's atmosphere, which distorts images and absorbs significant light, particularly in the EUV and X-ray wavelengths. This provides us a much clearer view of the Sun.

2.1.1 Solar and Heliospheric Observatory (SoHO)

SoHO is a joint mission between ESA and NASA launched in 1995 [16]. Also, it has three main instruments. 1- Large Angle and Spectrometric Coronagraph (LASCO): As we talked about previously, LASCO is a coronagraph that blocks out the bright disk of the Sun, letting us see the fainter corona in white light. It's amazing for spotting CMEs and other large-scale coronal structures [84,94,95]. 2- Extreme Ultraviolet Imaging Telescope (EIT): This instrument takes EUV images of the Sun, similar to SDO's AIA. It has fewer wavelength filters, but has been operating for many years and given us invaluable data [96]. Solar Ultraviolet Measurements of Emitted Radiation (SUMER): A spectrometer that measures EUV light and helps understand the temperatures, densities, and velocities of coronal plasma. SOHO has been essential in our understanding of the solar corona and how it interacts with the solar wind and the Earth [97,98]. It has given us a long-term view of solar behavior (https://sohowww.nascom.nasa.gov/).

2.1.2 Reuven Ramaty High Energy Solar Spectroscopic Imager (RHESSI)

A NASA mission launched in 2002 aimed to study solar flares. Although it is no longer operational, the data it collected has been invaluable. It has X-ray and Gamma-ray Spectrometer [99,100]. In fact, RHESSI's main instrument was designed to measure hard X-rays and gamma-rays emitted by the Sun, which are produced during solar flares. RHESSI was extremely good at studying flares in their highest energy emissions [101]. It has been essential to our understanding of how flares release energy (https://hesperia.gsfc.nasa.gov/).

2.1.3 Sun Watcher with Active Pixels and Image Processing (SWAP)

One of the significant EUV solar telescopes which is on board ESA's PROBA2 satellite is SWAP. It was designed to observe the Sun's middle corona (a region between the lower corona and outer heliosphere), it captures high-cadence, wide-field EUV images to study structures like coronal fans, eruptions, and EUV waves [102]. Using advanced active-pixel sensor technology, SWAP provides continuous, uncompressed observations, enabling long-term monitoring of solar activity across an 11-year solar cycle. Its innovations have significantly advanced understanding of dynamic processes in the Sun's extended atmosphere (http://proba2.sidc.be/swap).

In a review article conducted by [103], the authors provide a comprehensive survey of scientific contributions enabled by the SWAP. They synthesized research across three thematic areas: (1) long-lived structures like streamers, pseudo-streamers, and coronal fans; (2) dynamic phenomena such as eruptions, jets, EUV waves, and shocks; and (3) mechanisms driving coronal EUV emission generation. The review emphasized SWAP's pioneering role in advancing understanding of the middle corona – a previously underexplored region – and highlighted its innovative imaging techniques (e.g., off-limb enhancement methods) that improved observational clarity. By cataloging SWAP's legacy, the authors underscored its technical capabilities and lasting impact on solar physics, particularly in bridging gaps between low-corona and heliospheric studies.

2.1.4 Hinode

A Japanese mission with international (NASA/ESA) collaboration (launched 2006), dedicated to studying the Sun [19]. Its instruments are as follows: 1- EUV Imaging Spectrometer (EIS): It takes spectral measurements of the solar corona in EUV light, which helps to measure temperature, density, and velocity of the plasma [104]. 2- Solar Optical Telescope (SOT): It takes very high resolution images of the Sun in visible light [105–107]. 3- X-Ray Telescope (XRT): It takes images of the solar corona in X-rays [85,108]. It enables us to study the dynamics of various solar phenomena, particularly those originating in the photosphere (e.g., see [109–112]. Hinode helps us understand the dynamics of the Sun, its activity [113], and the connections between the different layers (https://hinode.nao.ac.jp/en/).

2.1.5 Solar Dynamics Observatory (SDO)

SDO is a NASA mission equipped with a comprehensive array of instruments designed to observe the Sun [20]. It's been a real workhorse since its launch in 2010. It involves three main instruments. 1- Atmospheric Imaging Assembly (AIA): This is the star of the show, taking high-resolution EUV images of the corona in multiple wavelengths. It has multiple filters, giving us access to a wide variety of plasma temperatures in the corona [83]. 2- Helioseismic and Magnetic Imager (HMI): This measures the Sun's magnetic fields and studies the interior of the Sun using waves that travel through it. It isn't technically measuring the corona, but the magnetic field that it observes is very important to understanding the corona [114,115]. 3- EUV Variability Experiment (EVE): This instrument measures the Sun's EUV irradiance. It does not make images, but measures the overall EUV output of the Sun, and helps to understand how that energy affects Earth [116]. SDO provides incredibly detailed images and data, helping us understand how the Sun's magnetic field affects the corona, solar flares, and CMEs. It gives us almost continuous coverage of the Sun (https://sdo.gsfc.nasa.gov/).

2.1.6 Parker Solar Probe

The Parker Solar Probe (PSP) is a NASA spacecraft launched in 2018 to study the Sun's outer corona. It's designed to get closer to the Sun than any previous mission, which allows it to gather unique data on solar wind and the Sun's atmosphere. the PSP doesn't have a traditional telescope. It's a spacecraft with in situ instruments. Its closest approach is < 10 solar radii (0.046 AU, or ~ 6.9 million km) from the Sun's surface [117,118]. It has some instruments: 1- FIELDS: Measures the 3-component electric and magnetic fields of the corona [119]. 2- Solar Wind Electrons Alphas and Protons (SWEAP): Analyzes solar wind particles (electrons, protons, and ions) [120]. 3- Integrated Science Investigation of the Sun (IS$\odot$IS): Detects energetic particles [121]. 4- Wide-field Imager for Solar PRobe (WISPR): Wide-field imager for coronal structures [122–124]. The main scientific goals are tracing the origin of the solar wind, coronal heating, studying magnetic field dynamics, plasma behavior, and dust populations (e.g., see [125–127]) near the Sun (https://science.nasa.gov/mission/parker-solar-probe).

2.1.7 Solar Orbiter (SolO)

ESA's mission, launched in 2020, to get closer to the Sun and observe it from different angles. It has provided valuable insights into the solar corona, including evidence linking coronal dimming to the Southern PCH [128]. It has some cool instruments for studying the corona [129,130]. It involves four types of instruments. 1- The Extreme Ultraviolet

Imager (EUI): Captures high-resolution images of the solar corona across multiple EUV wavelengths [131], enabling the characterization of transient phenomena such as small-scale brightenings [132,133]. 2- Spectrometer for Helioseismic and Coronal Explorer (SPICE): Measures the spectra of the solar corona in EUV light, to measure composition, temperature, and velocity of the plasma [134–136]. 3- Metis: A coronagraph instrument for imaging the corona in both polarized visible and UV light [137–139]. 4- Polarimetric and Helioseismic Imager (PHI): Takes images of the solar magnetic field [140,141]. Solar Orbiter is giving us new views of the Sun from different perspectives than we've seen before. It is helping us to understand how the Sun's magnetic field interacts with the corona (https://www.esa.int/Science_Exploration/Space_Science/Solar_Orbiter).

2.1.8 Aditya–L1

India's Aditya–L1 solar observatory, launched in 2023, hosts three advanced instruments for multi-faceted solar studies. The Aditya Solar wind Particle EXperiment (ASPEX) employs dual spectrometers (SWIS: 100 eV – 20 keV; STEPS: 20 keV/nucleon – 6 MeV/nucleon) to analyze solar wind protons, alpha particles, and energetic particles, with STEPS activated post-launch and delivering L1-consistent data [142]. The Fluxgate Magnetometer (MAG), positioned on a 6-m boom, measures interplanetary magnetic fields ($\pm$256 nT/axis at 125 ms intervals) to study space weather and detect CMEs, transmitting data daily via 12-hour ground windows [143]. Meanwhile, the Solar Ultraviolet Imaging Telescope (SUIT) captures full-disk and targeted solar imagery using 11 filters (200 – 400 nm), resolving magnetic coupling in the Sun's atmosphere and pioneering UV irradiance measurements critical for stratospheric ozone studies [144]. Each payload uniquely supports coordinated solar exploration at L1.

2.2 Ground-Based Telescopes and Instruments

Although they encounter atmospheric challenges, ground-based telescopes have some advantages, such as being easier to maintain and upgrade. They are also often useful for observing radio waves.

2.2.1 Coronal Multi-channel Polarimeter (CoMP)

A ground-based telescope located in Colorado, known as CoMP, specializes in observing the solar corona using polarized light across various wavelengths [145–147]. It measures the magnetic field of the corona and velocity of the plasma (https://www2.hao.ucar.edu/instruments/coronal-multi-channel-polarimeter-comp).

2.2.2 Owens Valley Solar Array (OVSA)

A radio telescope array in California, operated by the New Jersey Institute of Technology [148]. OVSA observes radio waves (1–18 GHz) emitted by the Sun, which allows scientists to study the acceleration of particles in solar flares and the structure of the corona [149,150] (https://www.ovsa.njit.edu/).

2.2.3 Atacama Large Millimeter/submillimeter Array (ALMA)

A large international radio telescope array in Chile. Though known for observing the distant universe, ALMA can also be used to observe the Sun at millimeter and submil-

limeter wavelengths [151,152]. This allows us to study the middle to lower solar corona (https://www.almaobservatory.org/en/).

2.2.4 Daniel K. Inouye Solar Telescope (DKIST)

A very large ground-based solar telescope located in Hawaii, operated by the National Solar Observatory. DKIST is still in the commissioning stage, but will give very high resolution observations of the Sun in many different wavelengths of light [153,154]. This will enable us to study the dynamics and magnetic fields of the photosphere and the corona, as well as how they interact. (https://nso.edu/inouye-solar-telescope/).

Numerous missions have been conducted to gather solar coronal data, utilizing a range of space- and ground-based instruments. For further study, readers may find more information from: The Advanced Solar Coronal Explorer Mission (ASCE) [155], Mirror Coronagraph for Argentina (MICA) [156], Giant Meterwave Radio Telescope (GMRT; see [157,158] and references therein), the Nancay Radio Heliograph (NRH) [159], Very High Angular Resolution Imaging Spectrometer (VERIS) [160], High-resolution Coronal Imager (Hi-C) [161,162] with its extended applications in Refs. [163,164], Magnetic Activity of the Solar Corona (MASC) [165], second flight of the Focusing Optics X-ray Solar Imager (FOXSI-2) [166], the Multi-Slit Solar Explorer (MUSE) (e.g., see [167–169] and references therein), Mauna Loa Solar Observatory (MLSO) [170], the Large Yield Radiometer (LYRA) (e.g., see [171,172]), the PArtially Multiplexed Imaging Spectrometer (PAMIS) [173], and the COronal Solar Magnetism Observatory (COSMO) [174].

3 Solar Coronal Data

As the solar corona is basically the outer atmosphere of the Sun, and it's super hot (millions of degrees), it emits light in different wavelengths, and that's what we use to study it. Each type of data – EUV, X-ray, white light, radio, and spectroscopic – provides us a different piece of the puzzle enhancing our understanding of the Sun's amazing complexity.

3.1 EUV Images

EUV light is invisible to the human eye, but it's perfect for seeing the hot plasma in the corona. These images are usually captured by satellites orbiting Earth or the Sun. EUV images are excellent for revealing the structure of the corona, including loops of magnetic fields, ARs (where sunspots are), and solar flares. It can be seen how the magnetic field is organized. Different wavelengths of EUV light will show different temperature plasma [175]. As some examples, a wavelength around 171 Å is often used to see material around 1 million Kelvin, which is good for seeing the general corona. A wavelength around 193 Å is good for seeing higher temperature plasma, often around 1.5 million Kelvin. Wavelengths around 94 Å show some of the hottest regions of the solar corona. Scientists use these images to study how energy moves through the corona and how solar storms form. They can see how those structures evolve over time. Also, EUV data is great for making movies. The interested reader can check out NASA's SDO [20], the AIA [83] section for a vast amount of EUV images (https://sdo.gsfc.nasa.gov/). Also, the European Space Agency's Solar Orbiter has some awesome EUV instruments, including the EUI [131] (https://www.esa.int/Science_Exploration/Space_Science/Solar_Orbiter).

3.2 X-Ray Images

X-rays are even higher energy than EUV, and they're emitted by the very hottest parts of the corona, like during solar flares. X-ray images are especially valuable for detecting non-thermal electrons [176] and intense solar flares that can affect Earth [177]. They also help reveal the most energetic plasma [178]. By analyzing X-ray data, scientists can study the process of how flares release significant amounts of energy and assess their potential impacts on our planet [179]. It can be observed the specific regions that are involved in the flare event, and follow how it evolves over time. The GOES (Geostationary Operational Environmental Satellite) satellites [180,181] are great sources of X-ray data [182]. The interested reader can check out their website for some information https://www.goes.noaa.gov/. The RHESSI spacecraft [99] was also a major player in X-ray studies of the Sun (https://hesperia.gsfc.nasa.gov/).

3.3 White Light Images

These are images of the corona in the visible light spectrum. However, since the corona is quite faint, they can usually only be observed during a total solar eclipse, or by using a coronagraph, which blocks out the Sun's bright disk so that we can see the dimmer corona [183,184]. White light images provide a view of the overall shape and structure of the solar corona (e.g., see [185], [186], and references therein for more details). You can see things like coronal streamers (those long, thin structures), and CMEs - those huge clouds of plasma being launched out into space [94,187,188]. These images are essential for understanding the large-scale dynamics of the corona, like where these big eruptions come from and where they are headed [189]. The LASCO instruments [84] on the SOHO (Solar and Heliospheric Observatory) spacecraft [16] have given us amazing white light images for many years (https://sohowww.nascom.nasa.gov/). Also, the STEREO (Solar Terrestrial Relations Observatory) mission [190] with a suite of scientific instruments (SECCHI: Sun Earth Connection Coronal and Heliospheric Investigation) [191] have white light coronagraphs too, allowing us to get a 3D view of the corona (https://stereo.gsfc.nasa.gov/).

3.4 Radio Observations

Radio telescopes are capable of detecting radio waves emitted by the solar corona (e.g., see [26]), providing valuable insights into its density and magnetic fields. These radio observations enhance our understanding of how particles are accelerated in the corona and allow us to observe details of solar bursts (e.g., see [192]) and their association with flares and CMEs. They also show different layers of the solar corona. Radio data gives us a unique look at the plasma in the corona, and gives us information that you can't get from EUV or X-ray images [193,194]. The Owens Valley Solar Array (OVSA) is a radio telescope [195,196] that's great for studying the Sun (https://www.ovsa.njit.edu/). Also, the ALMA can be used to study the Sun [151]. It is in the millimeter and submillimeter wavelength range, not just the radio range (https://www.almaobservatory.org/en/).

3.5 Spectroscopic Data

This data doesn't represent an image; it decomposes light into its various wavelengths. It's similar to observing a rainbow, but with much higher resolution than the human eye can perceive. The spectra allow scientists to measure the temperature, density, and velocity of the plasma in the corona [197]. Also, they can identify the different elements in the corona,

and figure out how much of each are there. Scientists can figure out the exact conditions of the plasma in the corona, which lets them understand how energy is transferred and how different structures are formed. The Hinode spacecraft has an EUV imaging spectrometer (e.g., see [104,198]) that gives some great information about the coronal plasma (https://hinode.nao.ac.jp/en/). The SUMER instrument [97,98] on SOHO was also a great source of spectroscopic data (https://sohowww.nascom.nasa.gov/).

4 Image Processing Methods

In the era of big data, image processing methods are indispensable in all fields of astronomy (e.g., see [199,200]) especially in solar data analysis. Solar observations, such as those from satellites like SoHO or SDO, generate vast volumes of high-resolution imagery that capture dynamic, complex phenomena (e.g., ARs, flares, coronal loops). Furthermore, raw solar data often contains noise, instrumental artifacts (e.g., limb brightening), and variations in brightness due to the Sun's spherical geometry or observational conditions [201]. It seems that the application of image processing techniques to solar data analysis dates back over three decades, with seminal works including: identification of CHs in X-ray and EUV coronal data [202,203], analysis of Yohkoh soft X-ray images [204–206], white-light image simulation of coronal structures recorded by solar probe [207,208], detection of emission regions using an Hα imaging coronagraph [209], emission measure variations in a QS [210], polarization observations of corona [211,212], topology of magnetic field lines [213].

Since the early 2000s, automated image processing methods have been increasingly employed to analyze solar atmospheric data. One of the first investigations of multiwavelength analysis in solar coronal, transition region, and chromospheric lines belongs to [214]. In this paper, the emissions of the QS from different instruments were collected and various image processing tasks like image reconstruction and cross-correlation method were employed to achieve statistical results. In article [215], the author developed a novel multi-exposure image compositing technique to capture the solar corona's intricate details across extreme brightness variations. In Ph.D. dissertation [216], the author leverages advanced image processing techniques (using such as modified Hough transform, automatic thresholding, and region-growing method) to study solar coronal dynamics, focusing on two phenomena: coronal loop waves using automated analysis of high-cadence EUV/SXR imagery (Part I), and CMEs applying detection method to coronagraphic white-light data (Part II). The dissertation advances solar image processing by bridging observational data [217] with theoretical models, enhancing the study of coronal waves and CMEs through automation and multi-instrument synergy.

In reference [218], the author addressed challenges in solar image processing, particularly flaws introduced by common re-sampling methods during tasks like co-alignment, reprojection, and solar rotation compensation. In this paper, it has been highlighted that while more accurate techniques, long established in computer graphics, exist to minimize distortion artifacts, these remain underutilized in solar physics. To bridge this gap, the author developed a mathematical framework for data re-sampling under arbitrary coordinate transformations and proposed an optimized algorithm like locally optimized spatial filtering to improve accuracy. They demonstrated the broader analytical potential of distortion techniques, such as enabling advanced image analysis beyond basic corrections. Examples were provided to illustrate how distortion can serve as a tool for scientific exploration. Finally, they introduced freely accessible software to empower the solar physics community with these refined methods, aiming to enhance data integrity and expand research capabilities.

In the other study [219], the authors developed an image processing method to isolate

solar dimmings from background noise and other structures. Here's a concise breakdown: 1- Fixed Difference (FD) Image Creation: Subtracted a pre-event baseline image from subsequent images to highlight dimmings, compensating for solar rotation to align structures accurately. 2- Threshold-Based Pixel Maps: (a) Maximal Pixel Map: Identified pixels below a weak threshold ($-\sigma$, where $\sigma \approx 150$ counts derived from pre-event FD histograms), capturing dimming regions but including noise. (b) Minimal Pixel Map: Selected the 1% darkest FD pixels to isolate core dimming areas, then applied 5×5 median filtering to remove small noise points, retaining only large, coherent structures. 3- Region-Growing with Constraints: Used the filtered minimal pixel map as seeds for region-growing, expanding only into pixels within the maximal pixel map. This ensured the final dimming region was simply connected (no isolated fragments) and excluded noise. 4- Noise Suppression: Combined statistical thresholding, median filtering, and connectivity constraints to distinguish true dimmings from transient artifacts, achieving precise spatial extraction of dimming regions. This approach involves dual thresholds and morphological filtering to balance sensitivity (maximal map) and specificity (minimal map), enhancing reliability in noisy solar imagery. The interested reader, also, can refer to the related papers such as [220,221] explaining exploration of EIT waves in the solar corona.

In [222], the authors developed an automated thresholding and region-growing (ATRG) method to detect ARs or plages in solar images from the EGSO Solar Feature Catalogue. Using Hα, Ca ii K3 (Meudon Observatory), and SOHO/EIT EUV data, their approach first segments solar images by defining local intensity thresholds for each quadrant to identify initial AR seeds. Median filtering and morphological operations refine the segmentation by removing noise and merging fragmented regions. Centroids of these regions act as seeds for region-growing, with dynamic local thresholds determining spatial boundaries. The automated results were compared to manually generated synoptic maps (Meudon Observatory and NOAA) over 2 months in 2002 and 5 years of data. While the method showed moderate correlation with manual detections, discrepancies highlighted inconsistencies in AR definitions across datasets, underscoring the need for standardized criteria. The work emphasizes improving reproducibility in solar feature identification through automated, statistics-driven techniques.

In the other work, the authors propose a segmentation method for detecting solar structures (e.g., CHs, ARs) in EUV images. Unlike conventional methods that rely solely on intensity, their approach integrates both intensity and multi-wavelength spectral data to account for luminosity variations. They demonstrate this using SOHO/EIT EUV images and employ a Bayesian classifier for supervised segmentation. The method is computationally efficient, enabling near-real-time tracking of dynamic solar features. By leveraging spectral information, it improves robustness against brightness fluctuations, offering a streamlined alternative to standard techniques [223].

In one of the studies related to identification of CMEs, the authors of [225] developed an automated image processing framework to detect, track, and visualize CMEs in coronagraph images, integrating physics-based criteria with computational techniques to address challenges such as noise suppression, dynamic feature evolution, and ambiguous boundaries. The pipeline began with preprocessing raw LASCO C2 images through exposure time normalization, noise filtering, and masking to remove cosmic rays, stars, and telemetry gaps, followed by polar coordinate transformation to align with the Sun's radial geometry. Initial detection leveraged running-difference images to isolate CMEs as bright leading edges, collapsing 2D angular-radial data into 1D intensity profiles and applying fixed thresholds to identify core angles representing the brightest regions. These angles were expanded via region-growing algorithms to estimate the full angular width of the CME, though limitations arose when overlapping events or deflected solar streamers complicated segmentation.

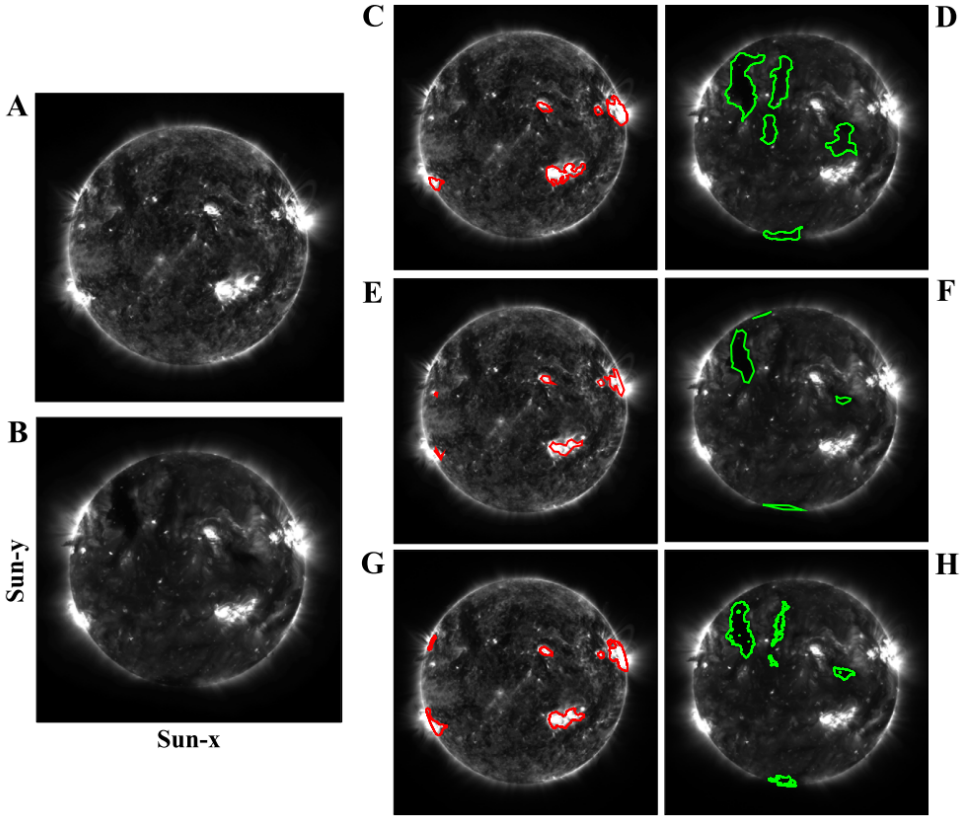

Figure 2: Full-disk SDO/AIA 171 Å (A) and 193 Å (B) observations from 25 June 2011 (13:00:36 UT) are shown. The top row (right panel) displays manually extracted AR (red contours, C) and CH (green contours, D) maps. The second row outlines SPoCA-derived AR (red, E) and CH (green, F) boundaries. The third row presents the proposed method's AR (red, G) and CH (green, H) detections using optimized (α, β) parameters. For further information, see [224]. Image reproduced with permission from [224], copyright by Springer.

Tracking relied on temporal coherence, requiring consecutive detections and radial projections to define the leading edge through iterative criteria: max-height (peak brightness) and half-max-lead/follow points were calculated, with constraints ensuring outward propagation by enforcing monotonic increases in height and distance between features. Successive images were analyzed chronologically, adjusting search boundaries and suppressing false signals from post-CME outflows using trailing-box masking and exponential smoothing. For visualization, the leading-edge shape was approximated by thresholding pixel intensities within an extended search region, applying mathematical morphology to remove noise and unify disjoint segments, then smoothing the upper boundary to outline the CME's diffuse front. The framework balanced sensitivity and specificity by iteratively refining thresholds and spatial constraints, though challenges persisted in distinguishing faint CMEs near bright events, resolving overlapping structures, and adapting to diffused or backtracking material. The integration of physics-driven assumptions – such as radial propagation and brightness-density correlations – with computational methods like coordinate transforms, adaptive masking, and morphological operations aimed to automate CME characterization while minimizing

artifacts, highlighting the iterative interplay between solar physics and algorithmic optimization in processing complex coronagraph data (e.g., see [226] and references therein).

In abstract [227], the authors developed a specialized method to track and visualized motion in solar corona image sequences. They first preprocessed individual frames by removing atmospheric light scattering, enhancing images via Gaussian filtering, and sharpening contours. Next, they analyzed the sequence by aligning clipped regions, creating maximal-brightness composite images, computing spatiotemporal gradients to determine motion direction, and visualizing movement through color hue and saturation shifts for each pixel.

One of the most fascinating studies of EUV image processing methods is work proposed by [228]. They developed a technique to detect polar coronal holes (PCHs) by adapting and refining existing techniques to account for challenges posed by solar limb geometry (which can be found in [229]) and variations in EUV emission. They selected daily solar EUV images near 0:00 UT across three wavelengths (171, 195, and 304 Å), calibrated them using standardized software (i.e., solar software abbreviated as SSW) to truncate pixel values between 0 and 1000, reducing storage demands without compromising detection. To enhance clarity, images underwent spatial smoothing via morphological operations – Erode, Dilate, Open, and Close – using a circular kernel to eliminate noise, BPs, and graininess while preserving large-scale features. Adaptive thresholding was applied using wavelength-specific intensity histograms to create binary images, isolating candidate PCH regions by setting thresholds at empirically derived levels (e.g., 30% darkest pixels for 171 Å) tailored to limb observations, intentionally overexposing equatorial regions to focus on polar boundaries. They shaped the Sun's visible surface into a ring covering the outer 6% of its radius. Areas beyond 60° latitude were blocked to focus on the polar regions. Detected hole edges were translated into Harvey coordinates, enabling perimeter tracking over solar rotation and aggregation over 33 days to map full boundaries and assess stability. Quality metrics discarded unreliable results (i.e., for instance, the percentage of pixels marked as CHs within the candidate hole boundary is considered less than 15% of all pixels in that region) to avoid false positives from equatorial intrusion during solar activity. Method verification involved simulating a synthetic CH with known parameters, testing detection accuracy under extreme projection effects, and validating robustness against rotational tilt and limb beveling. They studied the Sun's outer edge to avoid data distortion and used smart morphological filters to adapt to the variations of solar emission and measurement uncertainties.

In the study [230], the authors develop an image processing algorithm to detect low-contrast solar features (e.g., CHs, filaments) in radioheliographic data. Their method involves: 1- Noise reduction using an evolutionary Wiener-Tikhonov filter with adaptive parameters to smooth high-frequency noise while preserving structural details. 2- Contrast enhancement via a high-frequency (HF) filter that sharpens boundaries of low-contrast formations by amplifying brightness gradients. 3- Adaptive parameter selection, where filter settings (e.g., regularization strength, mask size) are dynamically adjusted based on the signal-to-noise ratio and spatial scale of the target features. 4- Software implementation to automate the process, enabling reliable isolation of structures like filaments and CHs in 5.2 cm wavelength radio images from the Siberian Solar Radio Telescope.

In dissertation [231], the author develop advanced image processing techniques to detect and analyze CMEs using data from the STEREO mission. First, multiscale methods were applied to coronagraph images to identify and track CME fronts, characterizing their shape as ellipses to precisely measure kinematics (e.g., acceleration) and morphology (e.g., angular width changes). Second, these methods were extended with 3-D reconstruction using dual-perspective STEREO observations, employing an elliptical tie-pointing technique to resolve the true geometry and propagation of CMEs beyond traditional 2-D plane-of-sky limitations.

Finally, this pipeline was automated to analyze large datasets, revealing key dynamics like early acceleration, non-radial motion, and aerodynamic drag in the solar wind, critical for improving space weather forecasting.

In the other related study, [232] built upon prior work by [233], who pioneered texture segmentation techniques on LASCO-C2 difference images to detect and track CMEs, demonstrating that texture analysis could quantitatively distinguish coronal events from the background. In this study, the authors focused on isolating coronal features through a bi-partitioning segmentation approach, framing the problem in computer-vision terms. They developed a supervised segmentation algorithm inspired by the region competition model, utilizing a level-sets technique to track the evolving CME front. This quasi-automated method required initial user input to define the CME boundary in the first image of a sequence, after which the algorithm autonomously propagated this boundary across subsequent frames. By leveraging texture characteristics derived from Gray Level Co-Occurrence Matrix (GLCM) analysis, the algorithm classified pixels as either belonging to the CME or the background. Their method involves segmentation Algorithm, GLCM implementation, and tracking, aimed to enhance objectivity in CME characterization by minimizing manual intervention while maintaining adaptability to dynamic coronal structures.

In the other study provided by [234], the authors developed a solar feature identification system that uses fuzzy logic principles (which handle uncertainty in data classification) to detect CHs and ARs in images captured by the SDO's AIA (SDO/AIA). Unlike traditional methods, their fuzzy-based approach enables efficient processing of solar images of varying sizes, making it both computationally lightweight and adaptable to different observational scales. The system prioritizes speed and flexibility while maintaining accuracy in identifying key solar structures.

In reference [235], the authors first cleaned up the solar image by replacing irregular negative pixels with zeros or nearby average values. They then created multiple Gaussian blur filters of different sizes (scales) to analyze the Sun's features. For each filter size, they calculated a "local average brightness" image and a "local brightness variation" image by comparing the original image to the blurred version. This allowed them to normalize the image at each scale, enhancing features relative to their surroundings. They applied an arctangent transformation to limit extreme values and repeated the process across multiple scales. Finally, they combined results from all scales (with optional weighting) and blended them with a globally adjusted version of the image to balance fine details and overall contrast, producing a clearer, more standardized solar image. The technique highlights small-scale details without losing context from larger structures, smooths out noise, exposes hidden features in faint outer regions (even at the image's edge), and was also tested effectively on white-light coronagraph data.

One of the robust application in the field of segmentation of ARs and CHs is the spatial possibilistic clustering algorithm (SPoCA) which is presented by [236] based on works done by [237] and [238]. In [237], the authors developed an unsupervised fuzzy clustering algorithm to automatically segment EUV solar images into three categories: CHs, QS, and ARs. The method uses multichannel data and incorporates spatial constraints to improve accuracy. Fuzzy logic handles uncertainties in image noise and ambiguous boundaries between solar regions. In the following of the prior work (i.e., SPoCA for segmenting solar EUV images into regions), [238] addressed limitations of SPoCA-notably, artifacts in results caused by the original method. The main improvements of the algorithm are optimizing clustering to better align with solar regions of interest, enhancing edge definition of clusters for sharper, more accurate boundaries, and introducing methodological extensions, such as automated AR tracking. At last, in [236], the authors introduce the SPoCA-suite, a comprehensive toolkit combining multiple clustering algorithms (e.g., Fuzzy C-means, Possibilistic

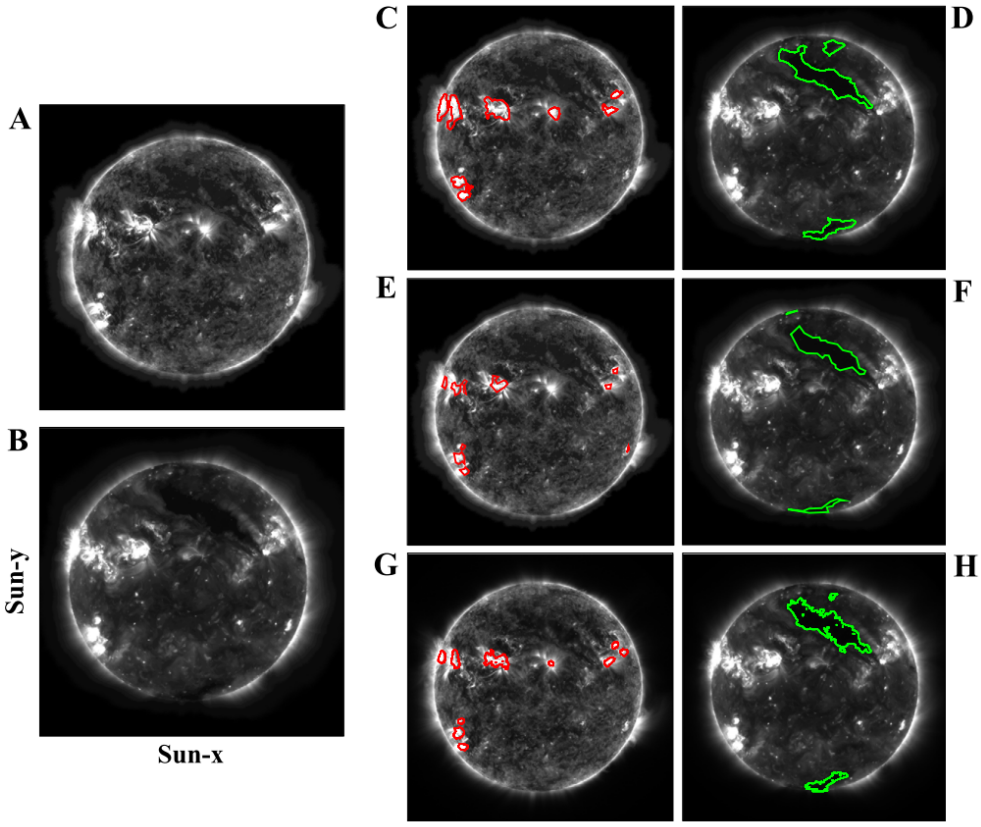

Figure 3: Full-disk SDO/AIA 171 Å (A) and 193 Å (B) observations from 28 July 2011 (13:00:37 UT) are shown. The top row (right panel) displays manually extracted AR (red contours, C) and CH (green contours, D) maps. The second row outlines SPoCA-derived AR (red, E) and CH (green, F) boundaries. The third row presents the proposed method's AR (red, G) and CH (green, H) detections using optimized (α, β) parameters. For further information, see [224]. Image reproduced with permission from [224], copyright by Springer.

C-means, SPoCA, and their variants) with pre- and post-processing routines to automatically detect and analyze solar features (i.e., ARs, QS, and CHs) in EUV images. Based on their prior works (which addressed artifacts and edge refinement), this suite integrates both fuzzy and possibilistic clustering methods, including histogram-based adaptations. The goal is to provide a consistent, automated framework for segmenting solar regions, enabling large-scale, systematic studies of their properties (e.g., evolution over time, intensity patterns). The SPoCA-suite employed fuzzy logic to handle noise and ambiguity in solar images, spatial constraints and probabilistic models to refine cluster accuracy, and automated workflows (pre/postprocessing) to standardize detection. The second rows of both Figures 2 and 3 show the SPoCA results for ARs (panel E) and CHs (panel F). Readers interested in SPoCA applications may refer to [172].

One of the automated approaches with acceptable accuracy has been proposed by [224] offered a robust tool for solar feature detection in EUV images. They developed an automated method to detect ARs in solar AIA 171 Å images and CHs in solar AIA 193 Å images using a Bayesian probabilistic framework combined with Markov-Gauss processes and Potts model

optimization. The process begins by assigning labels to pixels through weighted intensities of neighboring pixels, leveraging Markov-Gauss processes to model spatial dependencies. The image is then analogized as a lattice system, where pixel intensities and positions are treated as atomic states and locations, respectively. This framework allows the computation of Gibbs energy distributions and Hamiltonian terms via Markov random fields, represented as an undirected graph. To optimize pixel-state assignments, the method iteratively applies the Potts model, refining configurations to achieve the most coherent labeling (Figure 4). A cellular learning automaton is subsequently used to finalize label assignments, producing a binary image where interested areas (Ars or CHs) are marked as 1 and other regions as 0. To minimize false positives, a size threshold (> 1400 arcsec^2 for ARs and > 3000 arcsec^2 for CHs) is applied, filtering out small bright and dark regions, respectively, misclassified as ARs and CHs. However, the method has a limitation that there is slightly overestimation in number of areas compared to manual detection (differences $< 0.05\%$).

To compare the results of this method with the SPoCA outputs and manually detection benchmarks, [224] selected full-disk SDO/AIA images from two observation times: 25 June 2011 (13:00:36 UT) and 28 July 2011 (13:00:37 UT), captured at 171 Å (Figures 2A, 3A) and 193 Å (Figures 2B, 3B). ARs (Figures 2C, 3C) and CHs (Figures 2D, 3D) were first manually delineated. For comparison, the HEK catalog's SPoCA results (provided in [239]) at 171 Å (Figures 2E, 3E) and 193 Å (Figures 2F, 3F) were included. The authors of [224] then applied their method to these wavelengths, using optimized parameters (α, β), to extract ARs (Figures 2G, 3G) and CHs (Figures 2H, 3H), demonstrating its effectiveness relative to established techniques. Additional examples of segmented images including ARs and CHs are shown in Figures 5 and 6, respectively.

The validity of this method led to its use in [33] for statistical analysis of CHs during Solar Cycle 24, particularly around the solar maximum. The authors observe that large CHs do not form or vanish symmetrically in the Sun's northern and southern hemispheres. This asymmetry suggests differences in solar magnetic activity between the hemispheres. They also found that CHs tend to migrate toward the poles within their respective hemispheres over time, likely tied to the Sun's magnetic cycle dynamics. For more examples of CHs segmentation by the code presented by [224] see Figure 7.

In dissertation [240], an image segmentation method based on the Distance Regularized Level Set Evolution (DRLSE) framework was developed which is tailored for processing solar EUVI (Extreme Ultraviolet Imager) and magnetic field data. The standard DRLSE approach was modified by jointly analyzing both EUVI and magnetic images, ensuring segmentation respects physical boundaries by redesigning the edge function to prevent contour crossings over magnetic neutral lines (regions where the magnetic field polarity transitions). This adjustment forces the edge function to zero at neutral lines, effectively blocking contour evolution across these critical boundaries. To optimize parameters (α and σ derived from Gaussian function) controlling the segmentation sensitivity and smoothing, a training set was used to select median values via comparison with consensus maps. They were validated performance using leave-one-out cross-validation on a testing set. To address noisy derivatives in optimization, a robust pattern-search algorithm was employed to initialize with $\alpha = 0$ and $\sigma = 0.5$. They were accelerated convergence by initializing segmentations with the Henney-Harvey CH detection algorithm [229]. Additionally, a clustering step was introduced to merge closely spaced CHs (based on a pixel-distance threshold) to avoid fragmentation, ensuring robust detection and matching of features. The method has enhanced solar image analysis by integrating multi-modal data, preserving magnetic topology, and improving computational reliability for segmenting dynamic structures like CHs.

In reference [241], the authors developed a modular software framework to automate the detection, characterization, and tracking of solar features, addressing the challenge of

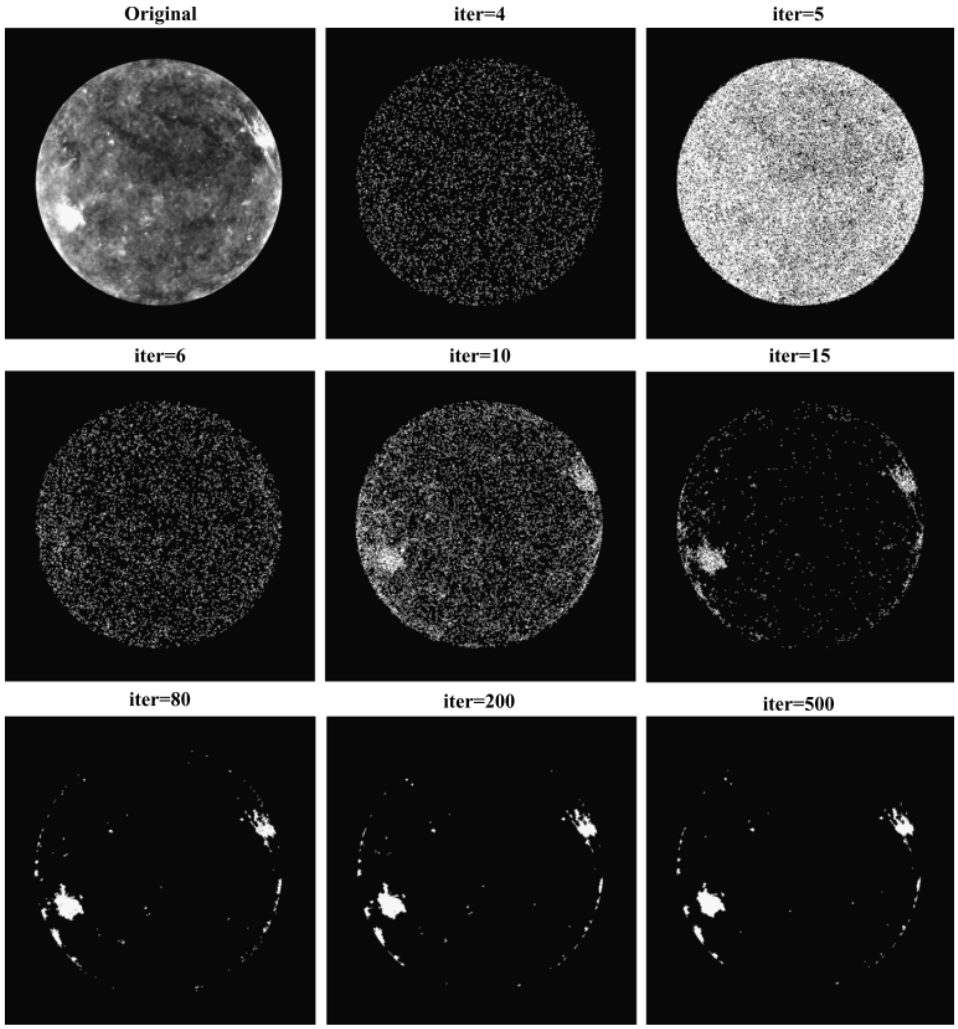

Figure 4: The first panel shows SDO/AIA 171 Å observations of ARs captured on 27 November 2010 at 08:23:13 UT, processed with varying iteration counts in the α and β parameter space. As iterations increase, AR structures are progressively identified, with filling factors stabilizing after approximately 400 iterations, beyond which no significant variation is observed. For details, refer to [224]. Image reproduced with permission from [224], copyright by Springer.

processing vast image datasets from missions like the SDO. Their approach combined a hybrid algorithm integrating the snake model – a boundary-delineation and tracking technique – with Particle Swarm Optimization (PSO), a stochastic optimization method known for efficiency in image analysis and dynamic problem-solving. This PSO-Snake model leveraged the snake model's precision in feature segmentation and PSO's adaptability to optimize tracking parameters, enabling automatic solar feature monitoring while capturing detailed characteristics. The framework was previously validated for tracking sunspots and coronal bright points, demonstrating robustness. In this study, the authors applied the PSO-Snake algorithm to calculate the solar corona's rotational velocity, comparing their automated

results against expert manual measurements to validate accuracy.

Among lots of software developed for detecting coronal features, there is an open-source Python tool, called the CHMAP (CH Mapping and Analysis Pipeline), to detect CHs in EUV images. Here is a concise explanation of how the CHMAP software works. It harmonizes EUV images from instruments like AIA/SDO and EUVI/STEREO-A to create unified, synchronic Carrington maps of the Sun. First, each raw image undergoes three critical preprocessing steps: 1- PSF Deconvolution: A GPU-accelerated correction sharpens features and reduces scattered light, enhancing image contrast. 2- Limb Brightening Correction: Using a six-month average of equatorial pixels, CHMAP flattens intensity variations from the Sun's center to its limb, preserving structures like ARs and CHs. 3- Inter-Instrument Transformation: A linear adjustment aligns brightness levels between different instruments, ensuring consistency. Once preprocessed, images are combined into a single Carrington map. CHs are then identified through an iterative thresholding scheme: a lower threshold "seeds" candidate regions, while a higher threshold refines their boundaries. This process accounts for intensity gradients and instrument differences, enabling precise, automated detection of CHs across the solar disk. The result is a standardized, multi-instrument view of CHs for analysis. The interested reader can be found the details of this method in [89,242].

One of the most interesting topics in the image processing field is motion magnification. Motion magnification, a technique to visualize subtle motions in videos, evolved from early works like [243], which relied on explicit velocity field estimation and frame warping but suffered from computational complexity and artifacts. [244] introduced Eulerian video magnification, bypassing motion estimation by applying spatial decomposition and temporal filtering to amplify small intensity changes and transverse motions, though it struggled with noise amplification and limited motion magnification. [245] improved this with a phase-based approach using complex steerable pyramids, amplifying temporal phase variations to enhance transverse motions selectively while preserving intensity and achieving higher magnification with better noise control. In work [246], the authors adapted these principles but replaced steerable pyramids with the dual-tree complex wavelet transform (DTCWT), leveraging its computational efficiency, shift invariance, and perfect reconstruction properties. Unlike prior narrowband-focused methods, their algorithm targets broadband motions – ideal for analyzing multi-modal, non-stationary oscillatory processes (e.g., decaying or modulated waves) common in solar structures (e.g., see [247]) – by amplifying a wider range of temporal frequencies, thus enhancing the study of dynamic solar phenomena like coronal loops and plasma flows.

Among lots of investigations for segmentation of coronal images, in paper [248], the authors developed a convolutional neural network (CNN) based on the U-Net architecture to segment CHs in solar images, adapting techniques from biomedical image processing to solar physics. They implemented a U-Net-like network with an encoder-decoder structure, where the input layer accepts 256×256-pixel grayscale solar images, and the output layer produces a segmentation map of the same dimensions, assigning probabilities (0 to 1) to each pixel for CH identification. The network architecture combines ConvBlocks – comprising two successive 3×3 convolutional layers with exponential linear unit (ELU) activation, zero padding, and dropout layers for regularization – to extract hierarchical features while minimizing overfitting. Spatial resolution is reduced via MaxPooling layers and later restored using TransposedConv layers (deconvolution with ELU activation), enabling the model to capture both broad context and fine localization details. Skip connections between the encoder (contraction path) and decoder (expansion path) integrate multi-scale feature maps, enhancing segmentation accuracy by preserving spatial context during upsampling. The final Conv layer employs a sigmoid activation to output pixel-wise probabilities, interpreted as the likelihood of CH membership. This approach leverages U-Net's proven ability in 2-D seg-

mentation tasks, optimizing it for solar data by balancing feature extraction, computational efficiency, and robustness to noise through dropout and specialized layer configurations.

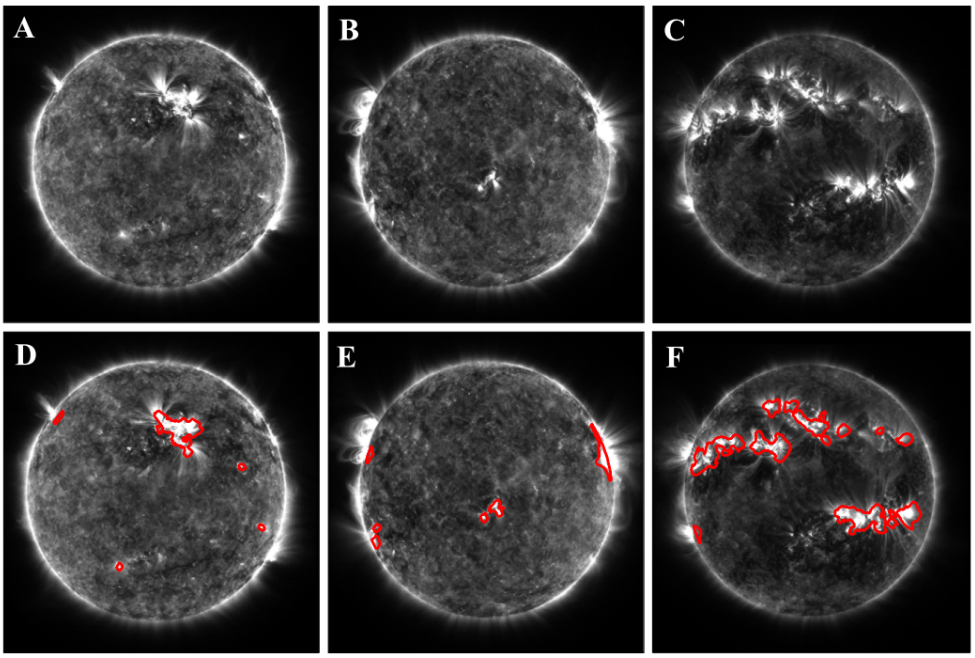

Figure 5: Additional examples of segmented images are provided, showcasing original 171 Å observations (panels A, B, C) alongside superimposed AR maps (panels D, E, F). These overlays illustrate the spatial correspondence between the raw data and the detected AR boundaries. The data correspond to observations from three dates: 22 January 2011 (left column), 24 February 2011 (middle column), and 31 March 2011 (right column). For more information, see [224]. Image reproduced with permission from [224], copyright by Springer.

In reference [249], the authors developed a fully automated image processing approach to analyze the cyclic latitudinal evolution of solar coronal ARs using daily SOHO/EIT images from 1995–2017. Their approach involved preparing and standardizing the image series, followed by histogram normalization and limb brightening correction to address observational intensity variations across the solar disk. In the next step, they segmented the images using intensity thresholds derived from histogram analysis to isolate ARs, transformed the segmented data into heliographic coordinates for spatial alignment with solar latitude-longitude grids, and systematically generated latitudinal distribution profiles for each daily observation. This method enabled consistent, long-term tracking of AR dynamics while minimizing manual bias, facilitating a robust analysis of their cyclic behavior over two solar cycles.

In the other novel work [250], the segmentation method applied to coronal images employs a neural network architecture called SCSS (solar corona structures segmentation)-Net, which combines an encoder-decoder structure for feature extraction and reconstruction. The encoder processes 256×256-pixel input images through five convolutional blocks, each containing two convolutional layers with 3×3 kernels, batch normalization, and ReLU activation, followed by max-pooling to reduce spatial dimensions. The number of filters increases from 32 to 512 across the blocks, enhancing hierarchical feature learning, while

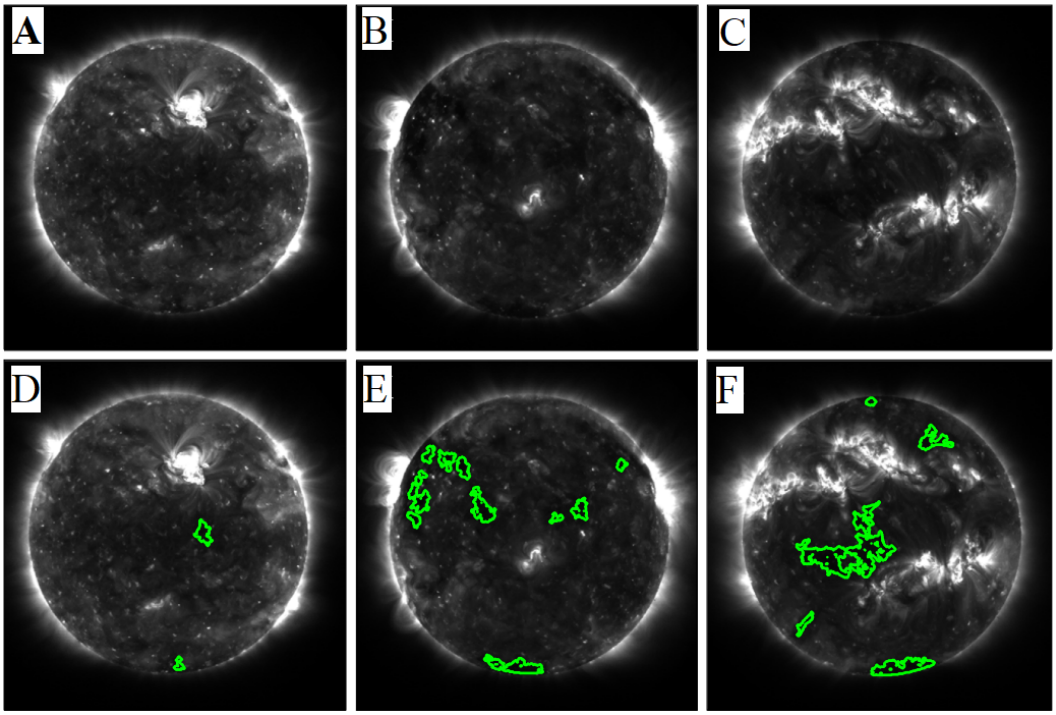

Figure 6: Additional examples of segmented images are provided, showcasing original 193 Å observations (panels A, B, C) alongside superimposed CH maps (panels D, E, F). These overlays illustrate the spatial correspondence between the raw data and the detected CH boundaries. The data correspond to observations from three dates: 22 January 2011 (left column), 24 February 2011 (middle column), and 31 March 2011 (right column). For further details, refer to [224]. Image reproduced with permission from [224], copyright by Springer.

dropout layers in the final three blocks mitigate overfitting by randomly deactivating units during training. The decoder mirrors this structure with four deconvolution blocks, using transposed convolutions and upsampling to reconstruct the spatial resolution, while skip connections concatenate encoder feature maps to decoder layers, preserving localization details. The network's output layer applies a 1×1 convolutional kernel with a sigmoid activation to produce pixel-wise binary classification (0 or 1) based on a threshold of 0.5, generating a segmentation mask that isolates coronal structures. Optimization leverages the Adam algorithm to minimize the binary cross-entropy loss, dynamically adapting learning rates using exponential moving averages of gradients and squared gradients. Performance is evaluated via the Jaccard index (Intersection over Union) and Dice coefficient (F1 score), which quantify overlap and similarity between predicted masks and ground truth. Regularization strategies include dropout layers and checkpointing to save models with minimal validation loss, ensuring robustness against overfitting. Hyperparameter tuning via grid search identified optimal settings: 256×256 input size, 0.5 dropout rate, batch size 20, and Adam optimization. The final output is a binary mask thresholded to distinguish foreground (coronal features) from background, enabling precise visualization of segmented structures overlaid on input images.

The authors of paper [251] developed an enhanced approach for mapping PCH boundaries by adapting and improving the perimeter-tracing algorithm originally introduced by [228] (as mentioned before). They translated the algorithm into Python, optimized it for parallel processing, and applied it to isolate PCHs by analyzing an annulus (ring-shaped region) near the Sun's limb. To address challenges caused by obscuration from EUV-emitting plasma – which varies with solar viewing geometry and plasma scale heights – the method employs morphological operations and an adaptive intensity threshold to define the hole boundary. To overcome ambiguity in edge detection due to differing observational wavelengths, the authors measured the PCH's boundary where it intersects the solar limb and tracked these positions over time as the Sun rotated. By aggregating limb measurements over 16.5 days (half a solar polar rotation), they reconstructed the full perimeter of the hole. Extending this to a full 33-day polar rotation allowed them to assess boundary stability by comparing two independent measurements of the same hole separated by 16.5 days, providing insights into temporal consistency and structural persistence of PCHs.

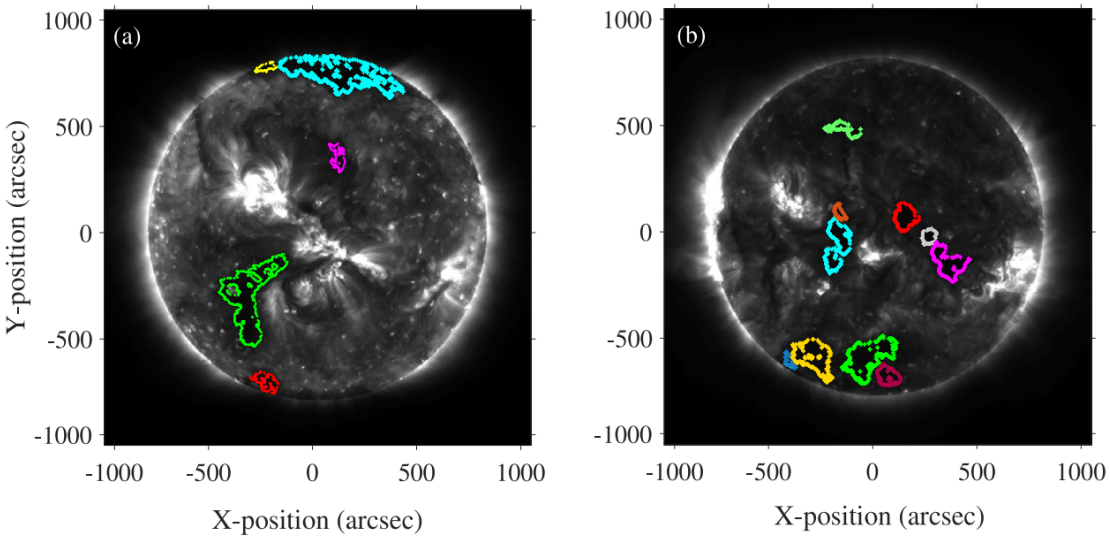

Figure 7: CH boundaries are superimposed onto full-disk AIA 193 Å images from two examples: 27 October 2017 at 22:10 UT (panel a) and 26 June 2014 at 05:00 UT (panel b). For more information, refer to [33]. Image reproduced with permission from [33], copyright by Elsevier.

In studying the Sun, tomography can combine images from multiple spacecraft (e.g., SOHO, STEREO) taken at different viewpoints to reconstruct the 3-D structure of CMEs or magnetic loops, enhancing understanding of solar dynamics. For instance, in references [252], the authors employed rotational tomography to validate the (Stanford and Michigan) MHD models of solar corona with the help of image processing methods such as using the normalizing-radial-graded filter (NRGF). In the other study [253], the authors use tomographic reconstruction techniques to create 3-D maps of the electron density and temperature in the solar atmosphere using processing methods like Ensemble Kalman Filter. This is achieved by combining 2-D images captured from multiple vantage points using ground-based and space-based instruments.In the following, the reader can find the 3-D tomography of the corona with different methods in references [254,255].

There are a set of useful references on these topics employed known image process-

ing methods in their works. A collection of this kind of studies are using the deconvolution techniques to correct stray light from EUV images of corona [256,257], employing the wavelet-based methods for both edge [258] and contrast enhancement [259], exploiting the normalized radial gradient filter to correct the radial intensity gradient [260], grasping the Fourier transformation and resampling filter to avoid introducing moiré artifacts [261], using the Hough transform to statistically characterize the herringbone morphology within a radio burst's fine structure [262], providing gradient images for tracking and mapping a motion [263], achieving intensity-based threshold for automatic detection of coronal brightenings for characterizing their released energy [264], convolving signal with some methods like using a narrow Gaussian kernel to preserve the events of interest at special ranges of frequencies [265,266], extracting intensity profiles of CBPs for finding their rotation [267], exploiting blind deconvolution associated with noise-adaptive fuzzy based equalization for image enhancement and then the cross-correlation registration [170], focusing on contrasting features extracted from "running difference" images – created by subtracting pixel intensities between consecutive time frames [90,268], using quantile radial normalization based on radial graded filter (RGF), and then, radial histogram equalizing filter based on RGF and adaptive histogram equalization for making images comparable with proposed model [269].

5 Conclusions

The solar corona, as the Sun's outermost atmospheric layer, remains a focal point for understanding solar dynamics and their profound influence on space weather. Advances in observational technologies, such as high-resolution imaging from spacecraft like the SDO and the PSP, have generated vast datasets that demand sophisticated image processing techniques to extract meaningful insights. Methodologies like contrast enhancement, multiscale filtering, and machine learning-driven event detection are indispensable for resolving the corona's faint structures – such as coronal loops, filaments, and eruptive events like solar flares and CMEs – against the Sun's bright background. These techniques not only improve the visibility of magnetic field configurations but also enable precise tracking of transient phenomena, which is critical for correlating coronal activity with in-situ solar wind measurements. By refining the interpretability of coronal images, such methods enhance space weather forecasting models, directly contributing to the protection of Earth's technological infrastructure, including satellites, power grids, and communication networks, from geomagnetic disturbances. Furthermore, integrating multi-wavelength data through co-registration algorithms provides holistic views of energy release mechanisms, advancing our grasp of coronal heating and solar cycle variability.

Despite these advancements, challenges such as data variability from observational constraints (e.g., atmospheric interference, spacecraft orbital limitations) and the computational demands of processing ever-growing datasets underscore the need for adaptive, scalable solutions. Future progress hinges on merging physics-based models with observational data, leveraging AI-driven analytics for real-time anomaly detection, and developing GPU-accelerated frameworks to handle large-scale data efficiently. These innovations will bridge gaps between theoretical predictions of coronal behavior and empirical observations, enabling more accurate forecasts of space weather events. Beyond solar physics, the methodologies developed for coronal image analysis – such as noise suppression and pattern recognition – hold transformative potential for exoplanetary research and astrophysical signal processing. As solar observation technologies continue to evolve, interdisciplinary collaboration across astrophysics, computer science, and space engineering will ensure that image processing remains central to unlocking the corona's mysteries. Ultimately, these efforts will not only

deepen our understanding of the Sun's influence on the solar system but also strengthen societal resilience to the Sun's dynamic outbursts, safeguarding critical infrastructure and fostering preparedness in an era increasingly reliant on space-based technologies.

Acknowledgment

We thank the Editorial Board of Iranian Journal of Astronomy and Astrophysics (IJAA) for giving us the opportunity of reviewing "Applications of Image Processing Methods in Solar Coronal Data Analyzes: An Overview". Also, the authors acknowledge "DeepSeek-R1-Lite-Preview" (an artificial intelligence (AI) assistant created exclusively by the Chinese Company **DeepSeek**) for assistance in refining the clarity and grammar of this manuscript. We extend our thanks to Iraj Safaei for granting access to the solar corona image (Figure 1) from his personal image library.

Authors' Contributions

All authors have the same contribution.

Data Availability

No data available.

Conflicts of Interest

The authors declare that there is no conflict of interest.

Ethical Considerations

The authors have diligently addressed ethical concerns, such as informed consent, plagiarism, data fabrication, misconduct, falsification, double publication, redundancy, submission, and other related matters.

Funding

This research did not receive any grant from funding agencies in the public, commercial, or nonprofit sectors.

References

[1] Pontin, D. I., & Priest, E. R. 2022, Living Reviews in Solar Physics, 19, 1.

[2] Kane, R. 2005, Advances in Space Research, 35, 866, fundamentals of Space Environment Science.

[3] Haigh, J. D. 2007, Living Reviews in Solar Physics, 4, 2.

[4] Pulkkinen, T. 2007, Living Reviews in Solar Physics, 4, 1.

[5] Kouloumvakos, A., Ph.D. thesis, University of Ioannina, Greece 2017.

[6] Wiegelmann, T., Thalmann, J. K., & Solanki, S. K. 2014, A&A Rev., 22, 78.

[7] Yang, Z., et al. 2020, Science, 369, 694.

[8] Phillips, K. J. H. 1995, Guide to the Sun,

[9] Dwivedi, B. N., & Parker, F. b. E. N. 2003, Dynamic Sun,

[10] Alzate, N., et al. 2017, ApJ, 848, 84.

[11] Hawass, Z. 2008, Tutankhamun and the Golden Age of the Pharaohs, National Geographic.

[12] Needham, J. 1959, Science and Civilisation in China, Vol. 3: Mathematics and the Sciences of the Heavens and the Earth, Cambridge University Press.

[13] Sun, X., & Kistemaker, J. 1997, The Chinese Sky During the Han: Constellating Stars and Society, Brill.

[14] Lyot, B. 1939, MNRAS, 99, 580.

[15] Golub, L., & Pasachoff, J. M. 2009, The Solar Corona.

[16] Domingo, V., Fleck, B., & Poland, A. I. 1995, Sol. Phys., 162, 1.

[17] Švestka, Z., & Uchida, Y. 1991, The YOHKOH (SOLAR-A) mission. A series of invited contributions.,

[18] Strong, K., et al. 1994, Space Sci. Rev., 70, 119.

[19] Kosugi, T., et al. 2007, Sol. Phys., 243, 3.

[20] Pesnell, W. D., Thompson, B. J., & Chamberlin, P. C. 2012, Sol. Phys., 275, 3.

[21] van de Hulst, H. C. 1950, Bull. Astron. Inst. Netherlands, 11, 135.

[22] Lamy, P. L., Gilardy, H., & Llebaria, A. 2022, Space Sci. Rev., 218, 53.

[23] Foukal, P. V. 2004, Solar Astrophysics,

[24] Aschwanden, M. J. 2005, Physics of the Solar Corona. An Introduction with Problems and Solutions (2nd edition).

[25] Priest, E. 2014, Magnetohydrodynamics of the Sun, Cambridge University Press.

[26] Mierla, M., et al. 2020, Sol. Phys., 295, 66.

[27] Dulk, G. A. 1985, ARA&A, 23, 169.

[28] Stix, M. 2004, The Sun: An Introduction.

[29] Owens, M. J., & Forsyth, R. J. 2013, Living Reviews in Solar Physics, 10, 5.

[30] Altrock, R. C. 2003, Sol. Phys., 216, 343.

[31] Cranmer, S. R. 2009, Living Reviews in Solar Physics, 6, 3.

[32] Gibson, S. E. 2018, Living Reviews in Solar Physics, 15, 7.

[33] Tajik, Z., et al. 2023, Advances in Space Research, 72, 1884.

[34] Klimchuk, J. A. 2006, Sol. Phys., 234, 41.

[35] Reale, F. 2014, Living Reviews in Solar Physics, 11, 4.

[36] McAllister, A. H., & Hundhausen, A. J. 1996, Solar Drivers of the Interplanetary and Terrestrial Disturbances, Vol. 95 of Astronomical Society of the Pacific Conference Series, edited by Balasubramaniam, K. S., Keil, S. L., & Smartt, R. N., 171.

[37] Lee, J.-O., et al. 2021, ApJ, 920, L6.

[38] Guo, W. P., & Wu, S. T. 1998, ApJ, 494, 419.

[39] Endeve, E., Holzer, T. E., & Leer, E. 2004, ApJ, 603, 307.

[40] Saito, T., Shibata, K., Dere, K. P., & Numazawa, S. 2000, Advances in Space Research, 26, 807.

[41] Abbo, L., Lionello, R., Riley, P., & Wang, Y. M. 2015, Sol. Phys., 290, 2043.

[42] Nakariakov, V. M., Pascoe, D. J., & Arber, T. D. 2005, Space Sci. Rev., 121, 115.

[43] Nakariakov, V. M., & Verwichte, E. 2005, Living Reviews in Solar Physics, 2, 3.

[44] Stepanov, A. V., Zaitsev, V. V., & Nakariakov, V. M. 2012, Coronal Seismology: Waves and Oscillations in Stellar Coronae Flare Plasma.

[45] Nakariakov, V. M., et al. 2016, Space Sci. Rev., 200, 75.

[46] Nakariakov, V. M., et al. 2021, Space Sci. Rev., 217, 73.

[47] Nakariakov, V. M., et al. 2022, Space Sci. Rev., 218, 13.

[48] Nakariakov, V. M., et al. 2024, Reviews of Modern Plasma Physics, 8, 19.

[49] Walsh, R. W., & Ireland, J. 2003, A&A Rev., 12, 1.

[50] Long, D. M., Ph.D. thesis, University of Dublin Trinity College, Ireland 2012.

[51] Marsch, E. 2006, Living Reviews in Solar Physics, 3, 1.

[52] van Driel-Gesztelyi, L., & Green, L. M. 2015, Living Reviews in Solar Physics, 12, 1.

[53] Toriumi, S., & Wang, H. 2019, Living Reviews in Solar Physics, 16, 3.

[54] Benz, A. O. 2017, Living Reviews in Solar Physics, 14, 2.

[55] Shibata, K., & Magara, T. 2011, Living Reviews in Solar Physics, 8, 6.

[56] Kowalski, A. F. 2024, Living Reviews in Solar Physics, 21, 1.

[57] Chen, P. F. 2011, Living Reviews in Solar Physics, 8, 1.

[58] Webb, D. F., & Howard, T. A. 2012, Living Reviews in Solar Physics, 9, 3.

[59] Kilpua, E., Koskinen, H. E. J., & Pulkkinen, T. I. 2017, Living Reviews in Solar Physics, 14, 5.

[60] Patel, R., Ph.D. thesis, University of Calcutta, India 2021.

[61] Zeighami, S., & Tavabi, E. 2023, Iranian Journal of Astronomy and Astrophysics, 10, 11.

[62] Chandrashekhar, K., et al. 2013, Sol. Phys., 286, 125.

[63] Alipour, N., & Safari, H. 2015, ApJ, 807, 175.

[64] Madjarska, M. S. 2019, Living Reviews in Solar Physics, 16, 2.

[65] Phillips, K. J. H., & Feldman, U. VizieR Online Data Catalog: Cool X-ray flares of Sun with GOES (Phillips+, 1995), VizieR On-line Data Catalog: J/A+A/304/563. Originally published in: 1995A&A...304..563P, 1995.

[66] Plutino, N., Berrilli, F., Del Moro, D., & Giovannelli, L. 2023, Advances in Space Research, 71, 2048.

[67] Hudson, H., et al. 2024, Sol. Phys., 299, 39.

[68] Watanabe, K., Masuda, S., & Segawa, T. 2012, Sol. Phys., 279, 317.

[69] Ursi, A., et al. 2023, ApJS, 267, 9.

[70] Berretti, M., et al. 2025, ApJS, 278, 9.

[71] Vakhrusheva, A. A., et al. 2024, Geomagnetism and Aeronomy, 64, 1.

[72] Kaportseva, K., Eremeev, V., Shugay, Y., & Kalegaev, V. 2022, 44th COSPAR Scientific Assembly. Held 16-24 July

[73] Otsu, N. 1979, IEEE Transactions on Systems, Man, and Cybernetics, 9, 62.

[74] Canny, J. 1986, IEEE Transactions on Pattern Analysis and Machine Intelligence, PAMI-8, 679.

[75] Adams, R., & Bischof, L. 1994, IEEE Transactions on Pattern Analysis and Machine Intelligence, 16, 641.

[76] Kalam, R., & Manikandan, K. 2011, 2011 International Conference on Process Automation, Control and Computing

[77] Vincent, L., & Soille, P. 1991, IEEE Transactions on Pattern Analysis and Machine Intelligence, 13, 583.

[78] Pereira, C. L., Bastos, C. A. C. M., Ren, T. I., & Cavalcanti, G. D. C. 2011, 2011 IEEE International Conference on Fuzzy Systems (FUZZ-IEEE 2011)

[79] Shi, J., & Malik, J. 2000, IEEE Transactions on Pattern Analysis and Machine Intelligence, 22, 888.

[80] Ronneberger, O., Fischer, P., & Brox, T. 2015, Medical Image Computing and Computer-Assisted Intervention – MICCAI 2015,

[81] S, M., et al. 2022, 2022 6th International Conference on Computing Methodologies and Communication (ICCMC)

[82] Karimi, D., Dou, H., & Gholipour, A. 2022, IEEE Access, 10, 29322.

[83] Lemen, J. R., et al. 2012, Sol. Phys., 275, 17.

[84] Brueckner, G. E., et al. 1995, Sol. Phys., 162, 357.

[85] Golub, L., et al. 2007, Sol. Phys., 243, 63.

[86] Aschwanden, M. J. 2010, Sol. Phys., 262, 235.

[87] Krista, L. D., McIntosh, S. W., & Leamon, R. J. 2018, The Astronomical Journal, 155, 153.

[88] Li, Q., et al. 2023, Sol. Phys., 298, 62.

[89] Heinemann, S. G., et al. 2023, A&A, 679, A100.

[90] Qu, M., Shih, F. Y., Jing, J., & Wang, H. 2006, Sol. Phys., 237, 419.

[91] Javaherian, M., & Eskandari, Z. 2023, Iranian Journal of Astronomy and Astrophysics, 10, 77.

[92] Javaherian, M., Safari, H., Amiri, A., & Ziaei, S. 2014, Sol. Phys., 289, 3969.

[93] Moradhaseli, M. A., Javaherian, M., Fathalian, N., & Safari, H. 2021, Acta Astron., 71, 163.

[94] St. Cyr, O. C., et al. 2000, J. Geophys. Res., 105, 18169.

[95] Mierla, M., et al. 2004, 35th COSPAR Scientific Assembly

[96] Delaboudinière, J. P., et al. 1995, Sol. Phys., 162, 291.

[97] Wilhelm, K., et al. 1995, Sol. Phys., 162, 189.

[98] Wilhelm, K., & Sumer Consortium 1997, Fifth SOHO Workshop: The Corona and Solar Wind Near Minimum Activity, Vol. 404 of ESA Special Publication, edited by Wilson, A., 17.

[99] Lin, R. P., et al. 2002, Sol. Phys., 210, 3.

[100] Hurford, G. J., et al. 2002, Sol. Phys., 210, 61.

[101] Lin, R. P., et al. 2003, ApJ, 595, L69.

[102] Berghmans, D., et al. 2006, Advances in Space Research, 38, 1807.

[103] West, M. J., et al. 2022, Sol. Phys., 297, 136.

[104] Culhane, J. L., et al. 2007, Sol. Phys., 243, 19.

[105] Tsuneta, S., et al. 2008, Sol. Phys., 249, 167.

[106] Ichimoto, K., et al. 2008, Sol. Phys., 249, 233.

[107] Suematsu, Y., et al. 2008, Sol. Phys., 249, 197.

[108] Kano, R., et al. 2008, Sol. Phys., 249, 263.

[109] Siarkowski, M., Falewicz, R., Kepa, A., & Rudawy, P. 2008, Annales Geophysicae, 26, 2999.

[110] Attie, R., Innes, D. E., & Potts, H. E. 2009, A&A, 493, L13.

[111] Winebarger, A. R., et al. 2012, ApJ, 746, L17.

[112] Hamedivafa, H. 2013, Sol. Phys., 286, 327.

[113] Imada, S., Kato, S., & Fujiyama, M. 2020, Sol. Phys., 295, .

[114] Scherrer, P. H., et al. 2012, Sol. Phys., 275, 207.

[115] Schou, J., et al. 2012, Sol. Phys., 275, 229.

[116] Woods, T. N., et al. 2012, Sol. Phys., 275, 115.

[117] Fox, N. J., et al. 2016, Space Sci. Rev., 204, 7.

[118] McComas, D. J., et al. 2019, Nature, 576, 223.

[119] Bale, S. D., et al. 2016, Space Sci. Rev., 204, 49.

[120] Kasper, J. C., et al. 2016, Space Sci. Rev., 204, 131.

[121] McComas, D. J., et al. 2016, Space Sci. Rev., 204, 187.

[122] Vourlidas, A., et al. 2016, Space Sci. Rev., 204, 83.

[123] Stenborg, G., et al. 2023, ApJ, 949, 61.

[124] Ascione, M. L., et al. 2023, AGU Fall Meeting Abstracts

[125] González, C. A., Verniero, J. L., Bandyopadhyay, R., & Tenerani, A. 2024, ApJ, 963, 148.

[126] Sterling, A. C., Panesar, N. K., & Moore, R. L. 2024, ApJ, 963, 4.

[127] Shen, M. M., et al. 2025, ApJ, 984, 165.

[128] Ngampoopun, N., et al. 2023, EGU General Assembly Conference Abstracts, EGU General Assembly Conference Abstracts

[129] Müller, D., et al. 2020, A&A, 642, A1.

[130] Harra, L., & Müller, D. 2025, Ap&SS, 370, 12.

[131] Rochus, P., et al. 2020, A&A, 642, A8.

[132] Chen, Y., et al. 2021, A&A, 656, L7.

[133] Narang, N., et al. 2025, arXiv e-prints, arXiv:2505.03656.

[134] Hassler, D. M. 2012, 39th COSPAR Scientific Assembly

[135] SPICE Consortium, et al. 2020, A&A, 642, A14.

[136] Fludra, A., et al. 2021, A&A, 656, A38.

[137] Antonucci, E., et al. 2020, A&A, 642, A10.

[138] Fineschi, S., et al. 2020, Experimental Astronomy, 49, 239.

[139] Romoli, M., et al. 2021, A&A, 656, A32.

[140] Solanki, S. K., et al. 2020, A&A, 642, A11.

[141] Loeschl, P., et al. 2024, A&A, 681, A59.

[142] Goyal, S. K., et al. 2025, Sol. Phys., 300, 35.

[143] Yadav, V. K., et al. 2025, Sol. Phys., 300, 33.

[144] Tripathi, D., et al. 2025, Sol. Phys., 300, 30.

[145] Tomczyk, S., et al. 2008, Sol. Phys., 247, 411.

[146] Fan, Y., Gibson, S., & Tomczyk, S. 2018, ApJ, 866, 57.

[147] Rumińska, A., Bak-Steślicka, U., Gibson, S. E., & Fan, Y. 2022, ApJ, 926, 146.

[148] Gary, D. E., et al. 2010, American Astronomical Society Meeting Abstracts #216, Vol. 216 of American Astronomical Society Meeting Abstracts, 405.20.

[149] Shaik, S. B., Gary, D., White, S., & Yu, S. 2023, 54th Meeting of the Solar Physics Division, Vol. 55 of AAS/Solar Physics Division Meeting, 112.03.

[150] Ashfield, W., et al. 2023, AGU Fall Meeting Abstracts

[151] Shimojo, M., et al. 2017, Sol. Phys., 292, 87.

[152] Carpenter, J. M., Corvillón, A., & Shah, N. B. 2025, PASP, 137, 034501.

[153] Rimmele, T. R., et al. 2020, Sol. Phys., 295, 172.

[154] Rast, M. P., et al. 2021, Sol. Phys., 296, 70.

[155] Kohl, J., et al. 1999, American Astronomical Society Meeting Abstracts #194, Vol. 194 of American Astronomical Society Meeting Abstracts, 65.06.

[156] Stenborg, G., et al. 1999, Solar Wind Nine, Vol. 471 of American Institute of Physics Conference Series, edited by Habbal, S. R., Esser, R., Hollweg, J. V., & Isenberg, P. A. AIP , pp. 561–564.

[157] Swarup, G. 2000, Geophysical Monograph Series, 119, 297.

[158] Kundu, M. R., et al. 2006, Sol. Phys., 236, 369.

[159] Mercier, C., et al. 2006, A&A, 447, 1189.

[160] Chua, D. H., et al. 2012, AGU Fall Meeting Abstracts

[161] Cirtain, J. W., et al. 2013, Nature, 493, 501.

[162] Winebarger, A. R., et al. 2014, ApJ, 787, L10.

[163] Brooks, D. H., Warren, H. P., Ugarte-Urra, I., & Winebarger, A. R. 2013, ApJ, 772, L19.

[164] Scullion, E., Rouppe van der Voort, L., Wedemeyer, S., & Antolin, P. 2014, ApJ, 797, 36.

[165] Auchere, F., et al. 2014, 40th COSPAR Scientific Assembly

[166] Ishikawa, S.-n., et al. 2017, Nature Astronomy, 1, 771.

[167] Tarbell, T. D., & De Pontieu, B. 2018, 2018 Triennial Earth-Sun Summit (TESS),

[168] De Pontieu, B., Lemen, J., Cheung, M., & Boerner, P. 2021, 43rd COSPAR Scientific Assembly. Held 28 January - 4 February

[169] De Pontieu, B., et al. 2022, ApJ, 926, 52.

[170] Liang, Y., et al. 2021, MNRAS, 503, 5715.

[171] Benmoussa, A., et al. 2009, A&A, 508, 1085.

[172] van der Zwaard, R., et al. 2021, Sol. Phys., 296, 138.

[173] Habbal, S., Ding, A., Yamashiro, B., & Nassir, M. 2022, Third Triennial Earth-Sun Summit (TESS)

[174] Tomczyk, S., et al. 2022, Third Triennial Earth-Sun Summit (TESS)

[175] Boerner, P., et al. 2012, Sol. Phys., 275, 41.

[176] Krucker, S., et al. 2008, A&A Rev., 16, 155.

[177] Holman, G. D., Sui, L., Schwartz, R. A., & Emslie, A. G. 2003, ApJ, 595, L97.

[178] Hudson, H. S. 2017, AGU Fall Meeting Abstracts

[179] Caspi, A., Krucker, S., & Lin, R. P. 2014, ApJ, 781, 43.

[180] Donnelly, R. F., Grubb, R. N., & Cowley, F. C. Solar X-ray measurements from SMS-1, SMS-2, and GOES-1, information for data users, 1977.

[181] Loto'aniu, P., et al. 2017, EGU General Assembly Conference Abstracts, EGU General Assembly Conference Abstracts

[182] Thomas, R. J., Starr, R., & Crannell, C. J. 1985, Sol. Phys., 95, 323.

[183] Belík, M., Marková, E., & Druckmüller, M. 2006, Solar Activity and its Magnetic Origin, Vol. 233 of IAU Symposium, edited by Bothmer, V., & Hady, A. A., 251.

[184] Espenak, F. 2013, in Lessons from the Masters, ,

[185] Martišek, K., & Druckmüllerová, H. 2011, ApJS, 197, 23.

[186] Rušin, V., Prikryl, P., & Prikryl, E. A. 2020, MNRAS, 495, 2170.

[187] Kaufmann, P., et al. 2003, J. Geophys. Res. (Space Physics), 108, 1280.

[188] Telloni, D., et al. 2013, ApJ, 767, 138.

[189] Chen, B., Bastian, T. S., & Gary, D. E. 2014, ApJ, 794, 149.

[190] Kaiser, M. L., et al. 2008, Space Sci. Rev., 136, 5.

[191] Howard, R. A., et al. 2008, Space Sci. Rev., 136, 67.

[192] Nedal, M., Kozarev, K., Zhang, P., & Zucca, P. 2023, A&A, 680, A106.

[193] Bastian, T. S., Benz, A. O., & Gary, D. E. 1998, ARA&A, 36, 131.

[194] Kaufmann, P., et al. 2002, ApJ, 574, 1059.

[195] Hurford, G. J., & Gary, D. E. 1989, BAAS

[196] Hurford, G. J., & Gary, D. E. 1990, BAAS

[197] Stoeva, P. V., Stoev, A. D., & Kostadinov, I. N. 2006, Sun and Geosphere, 1, 64.

[198] Shin, J., et al. 2021, 43rd COSPAR Scientific Assembly. Held 28 January - 4 February

[199] Javaherian, M., Miraghaei, H., & Moradpour, H. 2023, AJ, 166, 124.

[200] Javaherian, M., Miraghaei, H., & Moradpour, H. 2024, Research in Astronomy and Astrophysics, 24, 095003.

[201] Stoev, A., et al. 2021, Education and Heritage in the Era of Big Data in Astronomy, Vol. 367 of IAU Symposium, edited by Ros, R. M., et al., 365.

[202] Vaiana, G. S., Krieger, A. S., & Timothy, A. F. 1973, Sol. Phys., 32, 81.

[203] Broussard, R. M., Underwood, J. H., Tousey, R., & Sheeley, N. R.Jr. 1976, BAAS

[204] Lantos, P., Alissandrakis, C. E., & YOHKOH Team 1996, Advances in Space Research, 17, 261.

[205] Aurass, H., & Klein, K. L. 1996, Advances in Space Research, 17, 269.

[206] Belien, A. J. C., et al. 1996, Computers in Physics, 10, 573.

[207] Patsourakos, S., & Vial, J. C. 1997, Robotic Exploration Close to the Sun: Scientific Basis, Vol. 385 of American Institute of Physics Conference Series, edited by Habbal, S. R. AIP , pp. 129–136.

[208] Vial, J.-C., Koutchmy, S., Habbal, S., & Cor-I Team 1998, Advances in Space Research, 21, 291, space based astronomy: ISO, AGN, radiopulsars and the sun.

[209] Niot, J. M., & Noëns, J. C. 1997, Sol. Phys., 173, 53.

[210] Krucker, S., & Benz, A. O. 1998, ApJ, 501, L213.

[211] Hu, Z., et al. 1999, Acta Astrophysica Sinica, 19, 89.

[212] Gabryl, J. R., Cugnon, P., & Clette, F. 1999, Contributions of the Astronomical Observatory Skalnate Pleso, 28, 216.

[213] Filippov, B. 1999, 8th SOHO Workshop: Plasma Dynamics and Diagnostics in the Solar Transition Region and Corona, Vol. 446 of ESA Special Publication, edited by Vial, J. C., & Kaldeich-Schü, B., 311.

[214] Benz, A. O., & Krucker, S. 1999, A&A, 341, 286.

[215] Fukushima, H. 2002, Report of the National Astronomical Observatory of Japan, 5, 131.

[216] Robbrecht, E., Ph.D. thesis, Royal Observatory of Belgium 2007.

[217] Robbrecht, E., & Berghmans, D. 2004, A&A, 425, 1097.

[218] DeForest, C. E. 2004, Sol. Phys., 219, 3.

[219] Podladchikova, O., & Berghmans, D. 2005, Sol. Phys., 228, 265.

[220] Zhukov, A. N., & Auchère, F. 2004, A&A, 427, 705.

[221] Gallagher, P. T., & Long, D. M. 2011, Space Sci. Rev., 158, 365.

[222] Benkhalil, A., Zharkova, V. V., Zharkov, S., & Ipson, S. 2006, Sol. Phys., 235, 87.

[223] DeWit, T. D. 2006, Sol. Phys., 239, 519.

[224] Arish, S., Javaherian, M., Safari, H., & Amiri, A. 2016, Sol. Phys., 291, 1209.

[225] Olmedo, O., et al. 2008, Sol. Phys., 248, 485.

[226] Iglesias, F. A., et al. 2024, Boletin de la Asociacion Argentina de Astronomia La Plata Argentina, 65, 17.

[227] Pavlova, P., & Koleva, K. 2009, Publications of the Astronomical Society "Rudjer Boskovic", 9, 207.

[228] Kirk, M. S., Pesnell, W. D., Young, C. A., & Hess Webber, S. A. 2009, Sol. Phys., 257, 99.

[229] Henney, C. J., & Harvey, J. W. 2005, Large-scale Structures and their Role in Solar Activity, Vol. 346 of Astronomical Society of the Pacific Conference Series, edited by Sankarasubramanian, K., Penn, M., & Pevtsov, A., 261.

[230] Kuznetsova, S. M., et al. 2009, Geomagnetism and Aeronomy, 49, 850.

[231] Byrne, J. P., Ph.D. thesis, University of Dublin Trinity College, Ireland 2010.

[232] Goussies, N., Stenborg, G., Vourlidas, A., & Howard, R. 2010, Sol. Phys., 262, 481.

[233] Goussies, N. A., Mejail, M. E., Jacobo, J., & Stenborg, G. 2010, Pattern Recognition Letters, 31, 496, cIARP 2008: Robust and Efficient Analysis of Signals and Images.

[234] Colak, T., & Qahwaji, R. 2013, Sol. Phys., 283, 143.

[235] Morgan, H., & Druckmüller, M. 2014, Sol. Phys., 289, 2945.

[236] Verbeeck, C., Delouille, V., Mampaey, B., & De Visscher, R. 2014, A&A, 561, A29.

[237] Barra, V., Delouille, V., & Hochedez, J.-F. 2008, Advances in Space Research, 42, 917.

[238] Barra, V., Delouille, V., Kretzschmar, M., & Hochedez, J. F. 2009, A&A, 505, 361.

[239] Hurlburt, N., et al. 2012, Sol. Phys., 275, 67.

[240] Jatla, V. 2022, arXiv e-prints, arXiv:2207.10070.

[241] Shahamatnia, E., Dorotovič, I., Fonseca, J. M., & Ribeiro, R. A. 2016, Journal of Space Weather and Space Climate, 6, A16.

[242] Caplan, R. M., Downs, C., & Linker, J. A. 2016, ApJ, 823, 53.

[243] Liu, C., et al. 2005, ACM SIGGRAPH 2005 Papers, SIGGRAPH '05

[244] Wu, H.-Y., et al. 2012, ACM Trans. Graph., 31, .

[245] Wadhwa, N., Rubinstein, M., Durand, F., & Freeman, W. T. 2013, ACM Trans. Graph., 32, .

[246] Anfinogentov, S., & Nakariakov, V. M. 2016, Sol. Phys., 291, 3251.

[247] Gao, Y., Tian, H., Van Doorsselaere, T., & Chen, Y. 2022, ApJ, 930, 55.

[248] Illarionov, E. A., & Tlatov, A. G. 2018, MNRAS, 481, 5014.

[249] Maghradze, D. A., et al. 2020, Advances in Space Research, 65, 1321.

[250] Mackovjak, Š., Harman, M., Maslej-Krešňáková, V., & Butka, P. 2021, MNRAS, 508, 3111.

[251] Kirk, M. S. F., et al. 2022, Sol. Phys., 297, 42.

[252] Vásquez, A. M., et al. 2008, ApJ, 682, 1328.

[253] Butala, M. D., Kamalabadi, F., Frazin, R. A., & Chen, Y. 2008, IEEE Journal of Selected Topics in Signal Processing, 2, 755.

[254] Butala, M. D., Hewett, R. J., Frazin, R. A., & Kamalabadi, F. 2010, Sol. Phys., 262, 495.

[255] Wang, T., Jones, S. I., Arge, C. N., & Inhester, B. 2021, American Astronomical Society Meeting Abstracts, Vol. 238 of American Astronomical Society Meeting Abstracts, 328.07.

[256] Shearer, P., Frazin, R. A., Hero, A. O.III, & Gilbert, A. C. 2012, ApJ, 749, L8.

[257] Seaton, D. B., et al. 2013, ApJ, 777, 72.

[258] Morgan, H., Jeska, L., & Leonard, D. 2013, ApJS, 206, 19.

[259] Ko, Y.-K., et al. 2022, ApJ, 933, 95.

[260] Habbal, S. R., et al. 2013, Sol. Phys., 285, 9.

[261] DeForest, C. E., Howard, T. A., & McComas, D. J. 2014, ApJ, 787, 124.

[262] Carley, E. P., Reid, H., Vilmer, N., & Gallagher, P. T. 2015, A&A, 581, A100.

[263] Pavlova, P., Garnevski, D., & Koleva, K. 2016, Bulgarian Astronomical Journal, 24, 89.

[264] Joulin, V., Buchlin, E., Solomon, J., & Guennou, C. 2016, A&A, 591, A148.

[265] Morgan, H., & Hutton, J. 2018, ApJ, 853, 145.

[266] DeForest, C. E., et al. 2018, ApJ, 862, 18.

[267] Dorotovič, I., & Rybanský, M. 2019, Sol. Phys., 294, 109.

[268] Stupishin, A. G., Anfinogentov, S. A., & Kaltman, T. I. 2021, Geomagnetism and Aeronomy, 61, 1108.

[269] Gilly, C. R., Ph.D. thesis, University of Colorado, Boulder, Department of Astrophysical and Planetary Sciences 2022.